UNIVERSITÀ DEGLI STUDI DI PADOVA

UNIVERSITA' DEGLI STUDI DI PADOVA

Dipartimento di Ingegneria Industriale DII

Corso di Laurea Magistrale in Ingegneria Aerospaziale

Feasibility of Solar-Enhanced Thermoelectric Generators on Electrodynamic Tethers for Satellite Deorbiting

Relatore: Prof. Lorenzini

Correlatori: Prof. Tajmar, Ing. Peiffer

Giulia Bemporad 2053137

Anno Accademico 2023/2024

Abstract

In recent years, addressing the imperative of implementing a deorbit mechanism for satellite end-of-life scenarios has become a focal point in space studies. The E.T.Pack initiative actively contributes to this shared objective by proposing the use of an electrodynamic tether to generate a force for decelerating satellites. To achieve this, power is required to supply the electron emitter, enabling current flow through the tether.

This thesis explores a method to contribute a portion of the required power by incorporating a solar thermoelectric generator (TEG) onto the tether. TEGs are solid state devices based on the Seebeck effect, generating an electric potential difference when a temperature difference is established between two plates. Various TEG configurations such as bulk, y-type and planar are evaluated. Given the orbital motion, the flexibility needed for the deployment mechanism, the low thickness, and the twisting of the tether, the planar configuration is identified as the most viable option. Two different planar TEG manufacturing methods were studied, screen printing and sputtering deposition, and different institutes were contacted to receive samples of both types.

To achieve the temperature gradient in the planar configuration, strips of different optical properties are placed on the hot plate (a solar absorber with low emissivity) and on the cold plate (a solar reflector with high emissivity). This configuration ensures that the hot plate remains warmer than the cold plate, even without direct solar radiation, as it emits less heat than the cold plate.

Simulations involving radiative heat transfer were conducted to assess the achievable temperature gradient, and experiments in a vacuum chamber with solar simulator were carried out to evaluate the feasibility of the concept.

Sommario

L’implementazione di meccanismi per la deorbitazione dei satelliti al momento della fine della loro vita è diventata, negli ultimi anni, una ricerca fondamentale in ambito spaziale. L'iniziativa E.T.Pack contribuisce attivamente a questo obiettivo comune, proponendo l'uso di un nastro elettrodinamico per generare una forza di decelerazione sui satelliti. Per raggiungere questo scopo, è necessaria energia che alimenti l'emettitore di elettroni, così da consentire il flusso di corrente attraverso il nastro.

Questa tesi studia un metodo per fornire una parte dell'energia richiesta incorporando un generatore termoelettrico (TEG) solare sulla superficie del nastro. I TEG sono dispositivi a stato solido basati sull'effetto Seebeck, capaci di generare una differenza di potenziale elettrico quando viene stabilita una differenza di temperatura tra due piastre. Per questo uso, sono state valutate diverse configurazioni di TEG, come bulk, tipo y, planare. La configurazione planare è stata identificata come l'opzione più fattibile, considerando la traiettoria orbitale, la flessibilità necessaria al meccanismo di dispiegamento, il basso spessore, e la torsione del nastro. Sono anche stati studiati due diversi metodi di produzione dei TEG planari, stampaggio serigrafico e deposizione mediante sputtering, e sono stati contattati diversi istituti in modo da ricevere campioni di entrambi i tipi.

Per ottenere il gradiente di temperatura nella configurazione planare, strisce con diverse proprietà ottiche sono state collocate sulla piastra calda (un assorbitore solare con bassa emissività) e sulla piastra fredda (un riflettore solare con alta emissività). Questa configurazione assicura che la piastra calda rimanga più calda della piastra fredda, anche senza radiazione solare diretta, poiché emette meno calore rispetto alla piastra fredda.

Sono state condotte simulazioni che coinvolgono il trasferimento di calore radiativo per valutare il gradiente di temperatura ottenibile e sono stati effettuati esperimenti in una camera a vuoto con simulatore solare per valutare la fattibilità del concetto.

Table of Contents

Abstract 2

Sommario 3

Table of Contents 4

List of Figures 6

List of symbols 8

Abbreviations 9

1. Introduction 11

1.1 Importance of Deorbiting 11

1.2 E.T.Pack initiative 11

1.3 Employment of the tether surface 12

2. Fundamentals 13

2.1 Electrodynamic tethers 13

2.1.1 Anode and cathode 14

2.1.2 Tether deployment 15

2.1.3 Bare-photovoltaic-tether 15

2.2 Thermoelectric generator 16

2.2.1 Basic principles of thermoelectric energy generation 16

2.2.2 TEGs: state of the art 18

2.2.3 Planar μ-TEGs Manufacturing 21

2.3 Optically selective surfaces 23

3. Design process 24

3.1 Requirements 24

3.1.1 Dimensions and flexibility 24

3.1.2 Space environment 24

3.1.3 Power requirements 25
3.2 Preliminary design 25
4. Experiments 28
4.1 Objectives 28
4.2 TEGs Samples 28
4.2.1 IFW TEG 28
4.2.2 KIT TEG 33
4.2.3 IPF TEG 34
4.3 Optical surfaces samples 36
4.4 Instruments 37
4.5 Setup and procedures 40
4.5.1 Setup 40
4.5.2 Test of the optical surfaces 41
4.5.3 Test of the KIT TEGs 44
4.5.4 Test of the IFW TEG 48
4.5.5 Atomic Oxygen experiment 50
4.6 Summary and discussion of experiments results 51
5. Simulations 53
5.1 Objectives 53
5.2 Methods 54
5.3 Results and conclusions of the simulations 55
6. Conclusions and Outlook 57
References 60
Acknowledgements 65

List of Figures

Figure 2-1: Working principle of (top) C-EDT and (bottom) LWT System in retrograde orbit. [10] 13
Figure 2-2: Schematics of stationary spool (top) and rotating reel (bottom) configurations for the tape deployer. [10] 15
Figure 2-3: Schematic of a TEG device with a single thermoelectric couple and two legs. [14] 18
Figure 2-4: Vertical configuration on the left, planar configuration on the right. [16] 19
Figure 2-5: Hybrid configuration. [16] 19
Figure 2-6: Structure of Nguyen y-type TEG. [29] 21
Figure 3-1: Planar configuration with selective surfaces. 26
Figure 3-2: Vertical configuration on tether. 26
Figure 3-3: Planar configuration with legs encircling the tether. 27
Figure 4-1: IFW magnetron sputtering machine. 29
Figure 4-2: Leica LAS X microscope image of IFW TEG with silicon nitride on top. 30
Figure 4-3: Masks for the first TEG (measures in mm) 31
Figure 4-4: KIT TEG printed on Kapton (left) and on aluminum oxide (right). Below, examples of fracture are shown. 33
Figure 4-5: p-type material on the left and n-type material on the right. 34
Figure 4-6: TEG created with IPF materials and copper tape. 35
Figure 4-7: TiNOX reflectance spectrum. [43] 36
Figure 4-8: Layers that composes TiNOX material. [43] 37
Figure 4-9: Solar simulator. 39
Figure 4-10: Solar simulator and cold plate in the vacuum chamber. 40
Figure 4-11: Holders to keep the sample in place designed with SolidWorks. The part in light grey is in aluminum, the other is in PLA. 41
Figure 4-12: Samples to test the optical surfaces. Tether in stainless steel on the left and of aluminum on the right. The blue strip is TiNOX, the silver strip is anodized aluminum. 42
Figure 4-13: Results of the tests on the optical surfaces: on the left, there are the temperatures (green and light blue measured on the hot side, blue and orange on the cold side); on the right there are the gradients of temperature calculated using the average T. 43

Figure 4-14: Assembly of the 3 KIT samples. From left to right: A, B, C. 44
Figure 4-15: Comparison of gradient of temperature between the test with only Kapton and the test with aluminum substrate added underneath Kapton. 45
Figure 4-16: Sample A in vacuum: temperatures. 46
Figure 4-17: Sample A in vacuum: comparison between the trend of the T gradient and the trend of the maximum power point during the experiment. 46
Figure 4-18: Sample B graphics: on the top there is the comparison between the trends of temperature and MPP during the experiment in ambient air; on the bottom left there is the MPP trend during the experiment in vacuum; on the bottom right there is the comparison between I-V curves in air and in vacuum. 47
Figure 4-19: Assembly of the IFW sample. 48
Figure 4-20: Comparison between IFW TEG in vacuum and in ambient air. 49
Figure 4-21: Temperatures results for ambient air experiment. 49
Figure 4-22: Atomic oxygen machine on the left, positioning of the TEG on the right. 50
Figure 4-23: TEG before (right) and after (left) atomic oxygen exposure. The pictures on the bottom are taken with Leica LAS X microscope. 51
Figure 4-24: Detachment of TiNOX from the TEG. 52
Figure 5-1: Ansys thermal simulation of Al and optical selective surfaces when the sun in on the front. Temperatures are in Kelvin. 55
Figure 5-2: Ansys thermal simulations changing the thermal conductivity of the substrate. 237 W/m·K top left, 150 W/m·K top right, 100 W/m·K bottom left, 50 W/m·K bottom right. 56
Figure 6-1: Two strips of TEGs on the tether: future evaluation. 59

List of symbols

F	Flux of atoms
I	Current
PF	Power Factor
R	Resistance
$\mathbf{R_L}$	Resistance of the load
S	Seebeck coefficient
T	Temperature
$\mathbf{T_c}$	Temperature of the cold plate
$\mathbf{T_h}$	Temperature of the hot plate
V	Voltage
zT	Figure of Merit
$\boldsymbol{\alpha}$	Absorbance
$\boldsymbol{\alpha_{AB}}$	Seebeck coefficient
$\boldsymbol{\lambda}$	Thermal Conductivity
$\boldsymbol{\lambda_w}$	Wavelength
$\boldsymbol{\Delta T}$	Temperature gradient
$\boldsymbol{\varepsilon}$	Emissivity
$\boldsymbol{\eta_{bc}}$	Best Case scenario Efficiency
$\boldsymbol{\eta_{wc}}$	Worst Case scenario Efficiency
$\boldsymbol{\rho}$	Electrical resistance
$\boldsymbol{\sigma}$	Electrical conductivity
$\boldsymbol{\Phi}$	Flux density

Abbreviations

AM0	Air Mass 0
ATOX	Atomic oxygen
BPT	Bare Photovoltaic Tether
CAD	Computer-Aided Design
C-EDT	Cathode Electrodynamic Tether
CIGS	Copper–Indium–Gallium–Selenide
CNT	Carbon Nanotubes
CPC	Conductive Polymer Composites
DK	Deorbit Kit
DKD	Deorbit Kit Demonstrator
E.T.Pack	Electrodynamic Tether technology for PAssive Consumable-less deorbitKit
EDT	Electrodynamic Tether
FEA	Finite Element Analysis
GEO	Geostationary Earth Orbit
IADC	Inter-Agency Space Debris Coordination Committee
IFW	Leibniz Institute for Solid State and Materials Research
ILR	Institut für Luft- und Raumfahrttechnik
IoT	Internet of Things
IPF	Leibniz Institute of Polymer Research
KIT	Karlsruhe Institute of Technology
LEO	Low Earth Orbit
LWT	Low-Work-Function
MPP	Maximum Power Point
MWCNT	Multi-Walled Carbon Nanotubes
PF	Power Factor
PI	Polyimide
PLA	Polylactic acid
PTS	Photovoltaic Tether Segment
PVD	Physical Vapor Deposition
RF	Radio Frequency

RTG	Radioisotope Thermoelectric Generators
SCCM	Standard Cubic Centimeters per Minute
SMU	Source Measurement Unit
SoSi	Solar Simulator
S-S	Stainless Steel
STEG	Solar Thermoelectric Generator
SWCNT	Single-Walled Carbon Nanotubes
TC	Thermocouple
TEG	Thermoelectric Generator
TPU	Thermoplastic Polyurethan
Vac	Vacuum

1. Introduction

1.1 Importance of Deorbiting

Space is a naturally limited shared resource, and the number of launched satellites is constantly growing [1]. Every satellite left in space poses a hazard to other satellites, as it can lead to collisions, generating new, smaller, but dangerous debris. Therefore, it is of primary importance that, when a satellite concludes its mission, it leaves orbit in a short time. Currently, IADC Space Debris Mitigation Guidelines [2], involving most of the space agencies worldwide, stipulates that every satellite should deorbit or transit to a graveyard orbit within 25 years from the end of operations. However, there is a likelihood that this timeframe will be reduced to just 5 years [3], given the increasing concern about the debris problem.

Specifically, two regions, known as protected regions, are the most affected and require special attention: GEO (Geostationary Earth Orbit) and LEO (Low Earth Orbit). For this thesis, the focus is on the LEO region, which extends from Earth's surface up to an altitude of 2,000 km [2]. Many small satellites in the lower part of this region naturally decay in less than 5 years thanks to the aerodynamic drag [3], but there are still others that require deorbiting strategies.

Deorbit systems can be categorized as passive or active. The advantage of passive systems is that they require no further active control after deployment, making them the most used option for LEO satellites. The main types of passive systems include Drag Sails, Deployable Booms, and Electrodynamic Tethers (EDT) [3]. For the purpose of this discussion, the focus is on the latter.

1.2 E.T.Pack initiative

Recently, the European Commission funded the project called Electrodynamic Tether technology for PAssive Consumable-less deorbitKit (E.T.PACK) whose main objective is the preparation and commercialization of a set of products based on EDT technology. The goal of

developing a deorbit kit (DK) and related software with Technology Readiness Level 4 was achieved in 2022 [4], and now the team is continuing its work on the project. The DK should be designed to autonomously deorbit a spacecraft of 500 kg from a Sun-synchronous orbit of 850 km altitude in less than 24 months [5].

Currently, the E.T.PACK consortium is designing a Deorbit Kit Demonstrator (DKD) mission to be launched in 2025 with the objective to demonstrate the performances of the improved EDT solutions. The DKD has a standard 12U form factor, a mass of less than 24 kg and will be launched in a 600 km circular orbit with 51.5° inclination. The objective of the demonstration is to deorbit in less than 100 days, whereas the natural deorbit time would be of about 15 years. [6]

One partial aspect of the project is the enhancing of DK's power budget, by implementing additional power harvesting for the cathodic contact. One option is to explore the possibility of utilizing the surface of the tether.

1.3 Employment of the tether surface

In 2021, Tajmar and Sánchez-Arriaga proposed the bare-photovoltaic-tether (BPT) concept [7], aiming to take advantage of the progress in thin film solar cell technologies to use the surface area of the electrodynamic tether for solar energy harvesting. Modern EDTs use tapes instead of wires, due to enhanced performance and higher debris impact survival probabilities [8]. Since thin-film solar cells are flexible and can be manufactured with any desired length and the same cross-section dimensions as the bare segment (width around few centimeters and thickness of tens of microns), the resulting device is compact and preserves bare tether simplicity.

An alternative power harvesting solutions compatible with tethers was proposed, again by Tajmar, in 2023, that consisted in the implementation of thin-film flexible thermoelectric generators on the tether's surface, which is the focal point of this thesis and will be discussed in the following sections.

2. Fundamentals

2.1 Electrodynamic tethers

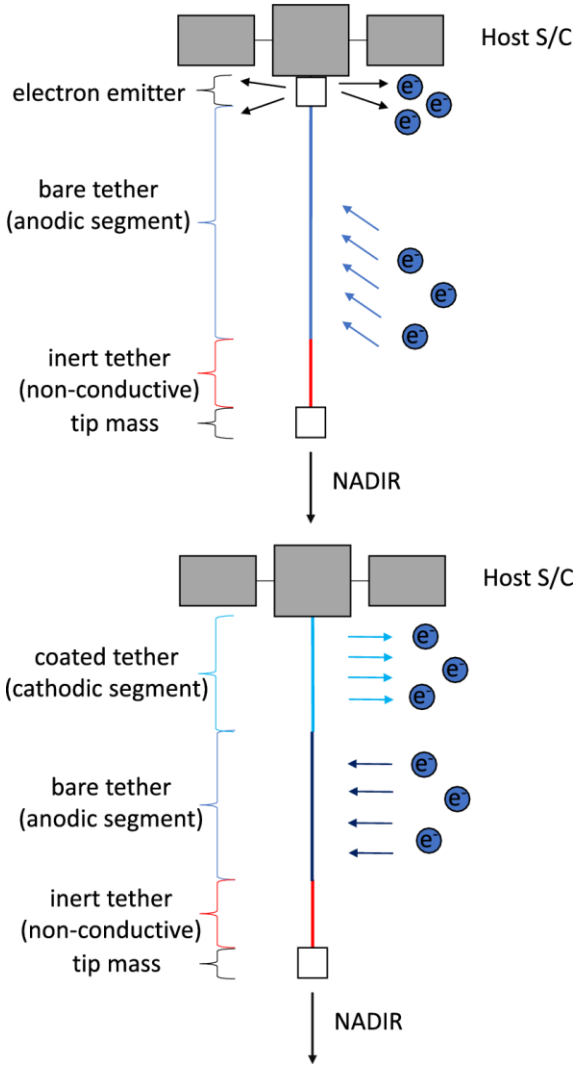

Figure 2-1: Working principle of (top) C-EDT and (bottom) LWT System in retrograde orbit. [10]

Electrodynamic tether (EDT) systems are a promising concept due to their potentially low mass, and, in comparison to drag augmentation devices, they demonstrate effectiveness across a broader range of altitudes. These are multi-kilometer conductive tape-shaped tethers

deployed from the satellite when deorbiting is required. The alignment is along the local vertical (nadir), taking advantage of the gravity gradient for stabilization.

Electrodynamic tethers function by collecting ionospheric electrons from the plasma environment (anodic contact), typically employing the bare tether principle [9]. To close the electrical circuit, these electrons are then re-emitted through a cathode (C-EDT) or a "Low-Work-Function" segment of the same tether (LWT). In both configurations, the resulting electric current flowing through the conductive tether generates a Lorentz force, thanks to the interaction with the Earth's magnetic field (Figure 2-1) [10]. This force can either generate thrust or drag, the latter gradually decreases the satellite's orbit altitude, ultimately leading to its re-entry into the atmosphere. [11]

2.1.1 Anode and cathode

The anodic contact is easy to passively operate, thanks to the above mentioned Bare Electrodynamic Tethers concept. A segment of the tether is left without insulation so that it can collect electrons from the plasma as a giant Langmuir probe [5].

On the contrary, the cathodic contact poses certain challenges. The idea of using a low-work-function material and use the passive thermionic and photoelectric effects to close the circuit is under development, but a coating with low enough work function has not been created yet [7]. The alternative is an active electron emitter, for which three major technologies are feasible: hollow cathode plasma contactor, thermionic electron emitter and field emission electron emitter. The former requires low amounts of power, but necessitates expellant gas, hence a pressure system and fluid channels. The latter two technologies are only available for low currents and require high amounts of power. This power requirement would compromise the compactness of autonomous EDT-based deorbit devices. For this reason, it is important to find a way to supply additional power to sustain the electron emitter. [12]

2.1.2 Tether deployment

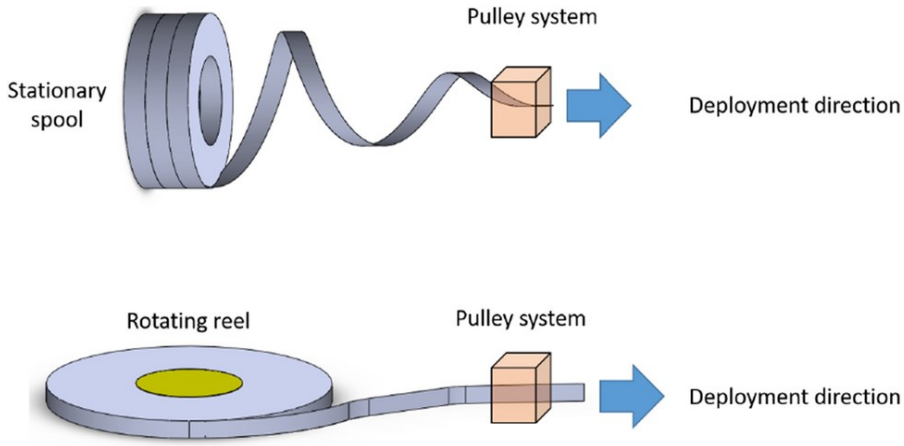

Figure 2-2: Schematics of stationary spool (top) and rotating reel (bottom) configurations for the tape deployer. [10]

The deployment mechanism is crucial as it affects the condition of the tether during its operation. In space tethers history, two main mechanisms have been used for tether deployment [13]: the rotating reel and the stationary spool (Figure 2-2). In 2020, Sarego et al. evaluated both options. Deploying from a stationary spool implies that the exiting tether undergoes a 360° torsional rotation per deployed turn, amounting to several thousand turns for a tether that is kilometers long. Thus, the reeling technology fits more readily with a tape-shaped tether, but the stationary spool has its own advantages over it (e.g. smaller size, no reel support, and bearings). The study concludes by selecting the stationary spool for a first E.T.PACK demonstration. [10]

2.1.3 Bare-photovoltaic-tether

In 2022, Peiffer and Tajmar conducted a feasibility study on the bare-photovoltaic-tether [12]. A Photovoltaic Tether Segment (PTS) measuring 3 m in length was manufactured, comprising submodules of 25 cm in parallel configuration. The I-V-characteristics of these submodules were measured under a Solar-Simulator inside a vacuum chamber, with temperatures ranging between -100°C and 100°C.

Applying thin film Copper–Indium–Gallium–Selenide (CIGS) solar cells to one side of a 2.5 cm wide and 40 μm thick aluminum-based EDT, assuming a power conversion efficiency of 5% for the PTS submodules, resulted in a power gain of 1.7 W/m at 25°C under full illumination (1367 W/m^2). However, the study reveals that the submodules' efficiency of the PTS has an average temperature coefficient of -0.45%/K, leading to a power loss of about 58% for an in-orbit operation temperature of 150°C. It's important to note that the 5% efficiency is attributed to an individual submodule, and an entire PTS with such high efficiency has not been manufactured, exacerbating the scenario.

The study also considered the twisting of the tether, which creates partial shading on the photovoltaic area. It is demonstrated that, in the best case, the total power of a (PTS) twisted uniformly along its entire length is reduced by a factor of $1/\pi$, and in the worst case, by a factor of 0.07, given the unpredictability of the twisting. This would result in an efficiency drop from $\eta_0 = 5$ % to $\eta_{bc} = 0.9\%$ (specific power 0.095 W/g) in the best-case scenario and to $\eta_{wc} = 0.2\%$ in the worst case (0.021 W/g).

The general orientation of the PTS in space is also a factor that was considered, depending on the orbital parameters of the spacecraft. This leads to periodic changes in tether illumination, that is rarely at its maximum. [12]

The conclusion of the study is that, at present, the bare-photovoltaic tether is feasible but insignificant in terms of energy harvesting for the cathode, that is the reason of the importance of the evaluation of the thermoelectric generators.

2.2 Thermoelectric generator

Thermoelectric generators (TEGs) are solid-state devices that converts thermal energy in electrical energy through a phenomenon called the Seebeck effect.

2.2.1 Basic principles of thermoelectric energy generation

In 1821, German physicist Thomas Seebeck discovered that when two wires made from dissimilar metals are joined at two ends to form a loop, and the two junctions are maintained at different temperatures, a voltage develops in the circuit. The two conductors are connected

electrically in series and thermally in parallel. The Seebeck effect appears due to the thermal diffusion which provokes the motion of the charge carriers (electrons or holes) across temperature difference in the conductors. [14]

The Seebeck voltage at the circuit junctions can be written as:

$$V = (\alpha_A - \alpha_B)(T_h - T_c) = S_{AB}\Delta T \qquad \text{Eq 2-1}$$

where α_A and α_B are the Seebeck coefficients for the conductors A and B (in V/K), T_h is the temperature of the hot plate and T_c the one at the cold plate. The Seebeck coefficient of a thermoelectric material or thermopower S_{AB} is the connection parameter between the input temperature difference and the output voltage difference. [14]

Thermoelectric materials

For efficient power conversion, the materials used in thermoelectric generators need to possess three main characteristics: a high Seebeck coefficient, low electrical resistance (ρ), and low thermal conductivity (λ). Therefore, the materials, in addition to having a high S, should also exhibit high electrical conductivity to prevent internal electrical losses, along with low thermal conductivity to allow the two plates to maintain a significantly different temperature. Meeting both requirements simultaneously is challenging due to the similar and linked thermal and electrical transport mechanisms.

Taking all these factors into account, the so-called figure-of-merit or zT-value is derived:

$$zT = \frac{S^2 T}{\rho\, \lambda} \qquad \text{Eq 2-2}$$

The temperature T appears in the formula because all the other elements are temperature-dependent. This is important because, during the evaluation, not only the temperature difference is to be taken into account, but also the working temperature range.

Today, semiconductors are the most used class of materials. In particular, n-doped semiconductors and p-doped semiconductors are associated, because n-doped materials have a negative Seebeck coefficient, and p-doped materials a positive one, resulting in a high S_{AB}.

The most used materials are Bi_2Te_3-based materials (bismuth telluride), because of their high figure of merit at ambient temperature. [15]

The simplest TEG consists of a thermocouple, comprising a pair of p-type and n-type legs (Figure 2-3). An electrical load having resistance R_L is connected in series with the output terminals of TEG, creating an electric circuit. [14]

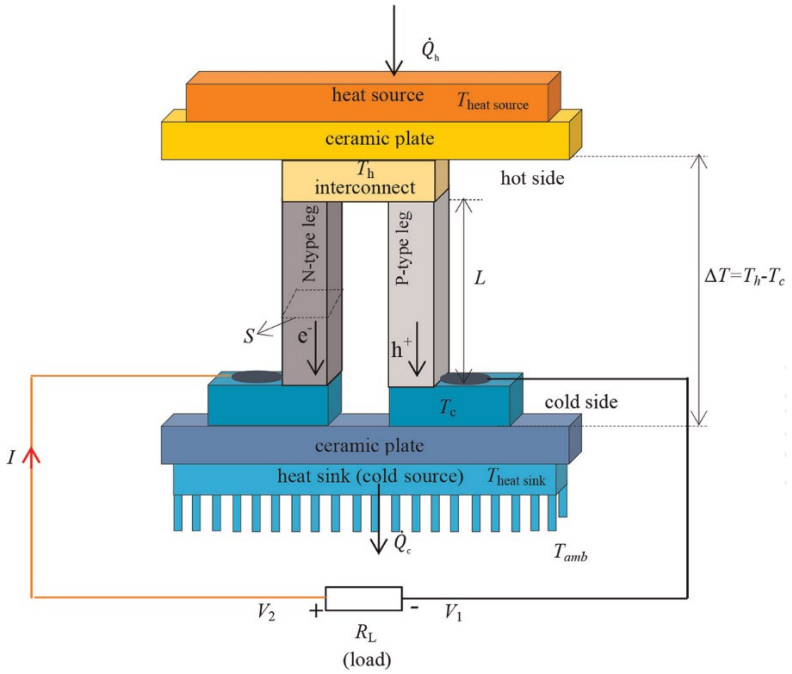

Figure 2-3: Schematic of a TEG device with a single thermoelectric couple and two legs. [14]

2.2.2 TEGs: state of the art

Given the thickness requirement of the tether, only thin TEGs are considered. Micro-Thermoelectric Devices (μ-TEDs) can generally be configured in three ways, depending on the layout of the thermoelectric legs and the direction of heat flow through the device during operation. The three configurations are: vertical/cross-plane (vertical), lateral/in-plane (planar), and lateral/cross-plane (hybrid). [16]

In the vertical configuration (Figure 2-4), thermoelectric legs are perpendicular to the substrate, and heat flows perpendicular to the device through area A. The advantages of this configuration are that it enables good thermal contact with the heat source/heat sink and a relatively high

packing density (the number of thermocouples per unit device area), thus enabling high power densities. However, only low temperature gradients can be realized because of the very low length of the legs.

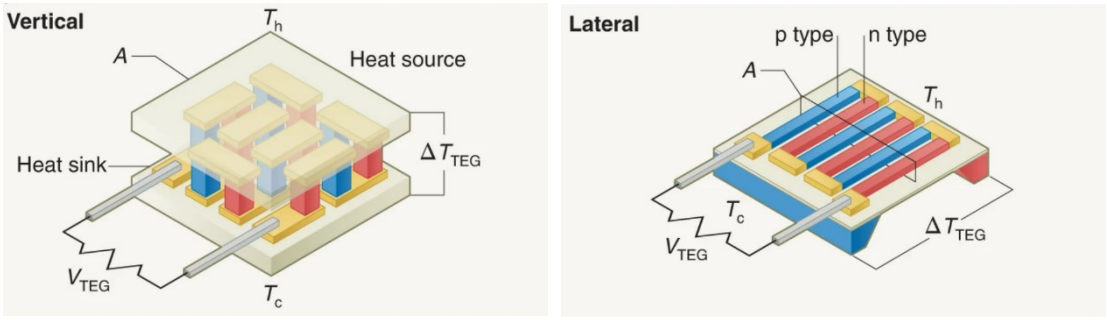

Figure 2-4: Vertical configuration on the left, planar configuration on the right. [16]

In the planar configuration, the heat flux is parallel to the device, allowing for much longer legs and the additional advantage of a simpler fabrication process. However, in this configuration, parasitic heat loss through the substrate can limit the output power. [16]

The hybrid configuration (Figure 2-5), also known as the y-type [16], can address the shortcomings of the vertical and lateral configurations because it has cross-plane heat flow achieved with laterally fabricated thermoelectric legs. Although this configuration can also suffer from parasitic heat loss through the substrate, high packing densities can be achieved.

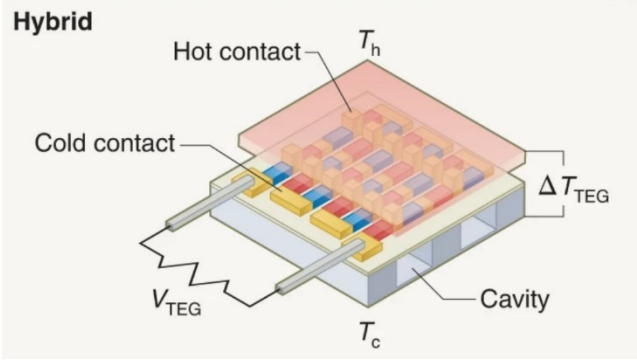

Figure 2-5: Hybrid configuration. [16]

TEGs in space

The first Thermoelectric Generators (TEGs) widely used in space are the Radioisotope Thermoelectric Generators (RTGs), first launched by the U.S. in 1961 and used ever since in many missions [17]. A radioisotope thermoelectric generator is a type of nuclear battery that utilizes the heat released by the decay of a suitable radioactive material to heat the hot plate of

a thermoelectric generator. While effective, radioactive sources are not practical due to the cost, complexity, safety, and legal challenges associated with radioactive material [18].

Another option is the Solar Thermoelectric Generator (STEG), which uses concentrated solar radiation as a heat source. For this, bismuth telluride is a favourable low-temperature (25– 225 °C) thermoelectric material, while filled-skutterudite is a good medium-temperature (25– 525 °C) thermoelectric material [18]. To concentrate the radiation, a focusing system is needed.

Both of these options are not of interest in this thesis since they are impossible to apply to the tether due to their complexity and dimensions.

Flat-plate Solar Thermoelectric Generators

NASA, in the 1950' with Telkes [19] and in the 1960' with Fuschillo and Gibson [20], proposed a flat-plate Solar Thermoelectric Generator for space applications without radioisotopes. Solar energy is absorbed by a sun-oriented plate of aluminum, coated to have a high absorptivity and a low emissivity. A similar plate, coated with a high emissivity surface, faces away from the sun, and radiates into space. In between, there are the thermoelectric legs in a classic vertical configuration. It is noteworthy that the temperature gradient is achieved also thanks to the differences in the optical properties of the two plates.

In more recent years, also Kraemer et al. [21] and Liu et al. [22] evaluated the use of flat-plate STEGs. Even if these devices are still bulk and not flexible, the use of optical surfaces can be studied also for other configurations.

Wearable devices

Most of the studies conducted in recent years regarding thin, flexible TEGs focus on wearable devices, which are essential components of the Internet of Things (IoT). These devices are utilized for environmental sensing and monitoring human health. The limited battery life of these electronics necessitates frequent recharging, posing a significant challenge. Therefore, researchers are exploring the integration of TEGs that harness the heat generated from the human body.

Most of them have a planar configuration and the most used semiconductor materials are Bi_2Te_3 ([23], [24]), SnTe/PtTe ([25]) and Ag_2Se ([26], [27]), while the material for the flexible substrate is usually polyimide (PI). The typical manufacturing methods are screen printing ([28]) and physical vapor deposition (PVD), by magnetron sputtering ([26], [27]) or evaporation ([23], [24]). They exhibit power densities ranging from of 0.1 to 100 mW/m^2, with temperature gradients between 50 and 150 K.

Regarding configurations other than the planar one, it's worth mentioning the work of Nguyen et al. in 2018 [29] that explore a hybrid configuration (y-type Figure 2-6).

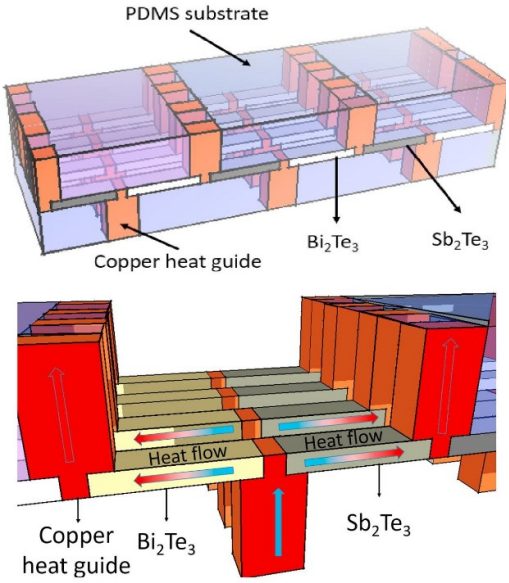

Figure 2-6: Structure of Nguyen y-type TEG. [29]

2.2.3 Planar µ-TEGs Manufacturing

For this thesis, the focus is on screen printing and magnetron sputtering, that are the techniques used for the manufacture of the TEGs tested in this work.

Screen Printing

Printing techniques are in development because they can reduce fabrication costs and simplify industrial scaling. Such techniques have the advantages of low-temperature vacuum-less

processes, low-cost equipment, low material wastage and suitability for a wide range of thermoelectric materials and substrates [16].

Basic screen printing consists of five main elements: screen mask (stencil), squeegee, press bed, printing ink and substrate [30]. The ink is poured onto the stencil and squeegeed to the substrate through it. As the screen and the substrate maintain a certain gap, pressing on the screen produces a reaction force that moves the contact line between the stencil and the substrate along the printing direction.

The main advantage of screen printing, compared to other printing methods, is the broader range of available substrates and inks that are compatible with this method [31].

Magnetron Sputtering

Sputtering is a plasma-based deposition process in which charged ions are accelerated toward a target containing the material to be deposited. The surface of the target is eroded, and the liberated atoms travel through a vacuum environment and deposit onto a substrate to form a thin film.

The sputtering gas is typically a high molecular weight gas such as argon or xenon. To initiate the process of plasma generation, high voltage is applied between the cathode, located behind the sputtering target, and the anode. The free electrons of the plasma move with high energy away from the cathode. When they collide with the gas, they knock other electrons off the atoms, causing ionization. At this point, the positive ions are accelerated toward the cathode, leading to high-energy collisions with the surface of the target. These collisions cause atoms at the surface of the target to be ejected into the vacuum environment with enough kinetic energy to reach the surface of the substrate and create the deposition layer. [32]

A magnetron sputtering source uses strong magnets to confine the electrons in the plasma near the surface of the target. This leads to a higher density plasma and increased deposition rates, but also prevents damage which would be caused by direct impact of these electrons with the substrate or the growing film [32].

These are the main advantages of this technique: it is compatible with lithography process (micro-structuring); composition and crystallinity can be tuned; pressure and power (and therefore sputtering rate) can be controlled; and, since there is vacuum, there is no oxidation.

The sputtering can be DC or Radio Frequency (RF). In RF sputtering, DC power source is replaced with an AC in which the polarity of the power supply changes alternatively at radio frequencies. This can avoid a charge building up on certain types of sputtering target materials, which over time can result in arcing into the plasma [33].

2.3 Optically selective surfaces

To achieve temperature gradients in certain types of TEG configurations, optically selective surfaces are required. These surfaces exhibit a particular emissivity spectrum.

Emissivity and absorption

Emissivity is defined as the amount of thermal radiation emitted or absorbed by a body compared to that of a black body under identical conditions [34]. The values range between 0 and 1. Among thermal radiations, visible radiation has a wavelength (λ_w) between 350 and 740 nm and infrared radiation has it between 740 nm and 15 μm [35]. Most radiation emitted by objects at room temperature falls within the infrared range, while most of the radiation from the Sun is in the visible range [34]. Therefore, when examining the wavelength spectrum of a material, the values of the coefficient over 740 nm are considered as emissivity (ε), and the values below 740 nm are treated as absorption (α) [36].

Some materials exhibit a variable spectrum [34]. Those with high emissivity throughout the entire λ_w range are called Flat Absorbers, those with low emissivity across all λ_w are called Flat Reflectors, those with low emissivity and high absorption are referred to as Solar Absorbers, and finally, those with high emissivity and low absorption are called Solar Reflectors [37].

The latter are widely utilized in aerospace applications; in fact, most visible surfaces of a spacecraft are coated with a thermal control finish [37]. Solar Reflectors are employed to prevent excessive heating, while Solar Absorbers are used to prevent excessive cooling.

3. Design process

3.1 Requirements

3.1.1 Dimensions and flexibility

Since the thermoelectric generators are to be placed on the EDT, they must meet certain requirements. First and foremost, there is a thickness requirement: the E.T.Pack tether is 40 μm thin [6] and, before deployment, is rolled onto a stationary spool [10]. Therefore, to avoid impediments and obstructions, the TEG should have a comparable thickness and high flexibility. The tether will be a 1200 aluminum alloy tape of 500 m with a width of 2.5 cm [6].

3.1.2 Space environment

The EDT is deployed when the satellite is in LEO, so the space environment must be considered.

The external thermal conditions include solar radiation, Earth's infrared radiation, and Earth albedo. Space is nearly equivalent to an absolute black body with a temperature of 2.725 +/- 0.002 K [38], acting as a heat sink. During the periodic motion of the satellite, mutual shadowing occurs among the spacecraft, Earth, and the Sun, as well as among different parts of the spacecraft. The ultra-high vacuum determines that thermal radiation is the primary mode of heat exchange between the space environment and the spacecraft [39]. Further evaluation on temperatures and heat transfer will be provided later on due to their significance in the functioning of TEGs.

Other ultra-high vacuum effects of interest are out-gassing, materials evaporation, sublimation, and decomposition [39].

In LEO, one of the dominant components of the atmosphere is atomic oxygen. It is formed through the photodissociation of residual diatomic oxygen exposed to the sun's ultraviolet radiation. LEO atomic oxygen is highly reactive and possesses sufficient energy to break

chemical bonds. It easily oxidizes all hydrocarbon-based polymers and graphite, leading to surface degradation [40].

Other potentially dangerous environmental characteristics are not discussed here, as the E.T.Pack mission is short enough to not be affected.

3.1.3 Power requirements

For the electron emitter of the DK, the power consumption is expected to be less than 10 W [6]. The TEG is expected to contribute a portion of the power required for the EDT, so even 1 W would be a significant aid for the E.T.PACK project. However, for the purpose of the thesis, the focus lies on assessing the feasibility of the concept. Therefore, every measurable power is to be considered a positive result, while still aiming for the highest possible power output.

3.2 Preliminary design

Planar flat-plate STEG

Considering the requirements and the state of the art, certain considerations have been made. Since most wearable devices are in a planar configuration, ensuring optimal thickness and flexibility, this thesis also begins with the evaluation of the planar configuration. Another important advantage of this configuration is its easy manufacturing.

Assuming a non-twisted tether, the issue with the planar configuration is that solar radiation would reach both the hot and cold plates with the same intensity, making it impossible, without any additions, to establish a temperature gradient between the two.

However, taking the example of the aforementioned flat-plate STEGs, there is the possibility of leveraging materials with different optical characteristics. Placing a Solar Absorber (high α, low ε) on the hot plate and a Solar Reflector (low α, high ε) on the cold plate would assure a temperature gradient between the two. The configuration is shown in Figure 3-1

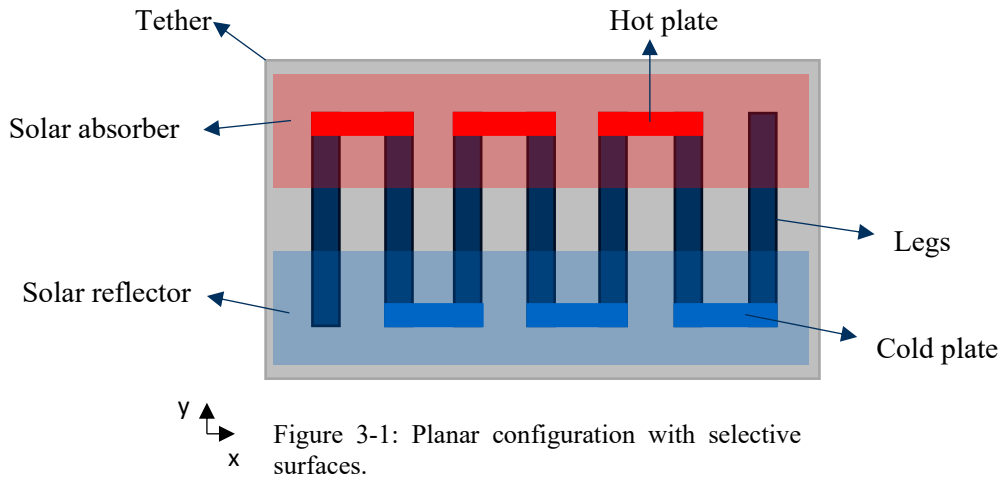

Figure 3-1: Planar configuration with selective surfaces.

A significant advantage of this configuration lies in the fact that the thermal gradient is not rapidly nullified even in full shadow. This is because the difference in emissivity leads to faster cooling of the cold plate compared to the hot one.

Other options

Other configurations were also evaluated, starting with the classical vertical configuration (Figure 3-2). Although the achievable thickness (tens or hundreds of micrometres [16]) in this type is greater than that of the planar configuration, for the purposes of this TEG, the thickness would still be sufficiently thin. However, the low thickness in this configuration not only increases manufacturing complexity but also impedes the achievement of a significant temperature gradient due to the short length of the TEG legs [16].

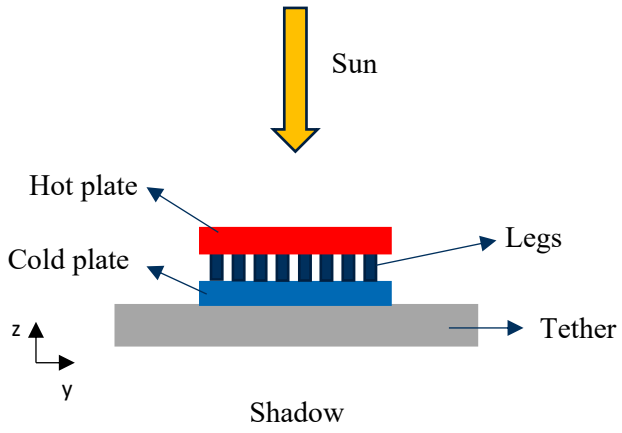

Figure 3-2: Vertical configuration on tether.

An advantage of this configuration is that when one side of the tether is illuminated by the sun, casting a shadow on the other side, the TEG's hot plate receives direct radiation, while the cold side is shielded. This has the potential to create a substantial temperature gradient. However, considering the twisting of the tether and the satellite's orbital motion, there will be periods during which the hot plate is in shadow, and the cold plate is exposed to sunlight. This inversion of the temperature gradient also inverts the potential gradient, leading to technical challenges. Furthermore, when the tether is completely in shadow, both plates rapidly reach the same temperature, leading to no energy harvesting. For the same reasons, also y-type configuration was excluded.

Another possible option is to use a planar TEG so that the hot plate would be on one side of the TEG and the cold one on the other, with the thermoelectric legs encircling the tether as shown in Figure 3-3. While this configuration could result in a potentially significant temperature gradient and would overcome the problem of short legs of the vertical configuration, it would still encounter the same issue of inversion described earlier.

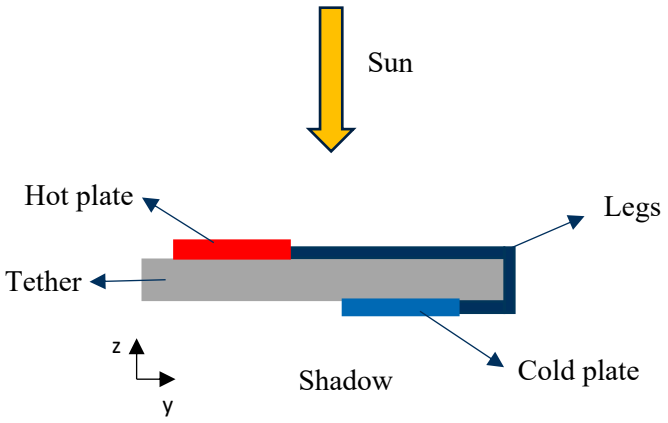

Figure 3-3: Planar configuration with legs encircling the tether.

4. Experiments

4.1 Objectives

The experiments were conducted to assess the feasibility of the concept, primarily to determine if the consistent difference in optical properties between the materials alone was adequate to generate a temperature gradient between the two plates. Additionally, there was interest in whether the temperature difference was sufficient to produce a notable power output from the thermoelectric generators. Some tests were conducted both in ambient air and in a vacuum to evaluate the impact of convection. Furthermore, temperature and power measurements were not immediately halted after turning off the SoSi, allowing for assessment of whether the gradients would persist for some time due to the differing emissivity of the two optical selective surfaces. The experiments also aimed to compare various types and materials of TEG samples, thanks to the assortment of samples available.

4.2 TEGs Samples

4.2.1 IFW TEG

Leibniz Institute for Solid State and Materials Research (IFW) is an institute located in Dresden. The microstructuring laboratory of the department of Metallic Material collaborated in this thesis by providing everything that was necessary for the production of a customized planar sputtered TEG. The Magnetron Sputtering machine used is the Compact Research Coater System CRC600 Series (Figure 4-1).

Figure 4-1: IFW magnetron sputtering machine.

Devices

Three devices were manufactured at IFW, all based on Bismuth Telluride and Antimony Telluride. Due to the dimensions of the manufacturing machines, the surface of the first IFW TEG is 4 cm x 2 cm. Instead of being sputtered onto an aluminum tether sample, the TEG is sputtered onto a stainless steel sample coated with a layer of aluminum oxide for electrical insulation. This choice is made due to the unavailability, within the required timeframe, of an aluminum tether with an insulating coating.

After careful observation, some cracks were found in the aluminum oxide layer, making it risky to sputter directly onto it. In fact, any electrical conduction through this substrate would completely compromise the functionality of the TEG. To address this issue, a 60 nm layer of silicon nitride was RF-sputtered on top of the 4 cm x 2 cm oxide-coated stainless steel sample.

Nevertheless, due to the roughness of the surface of the oxide, the sputtering process was not perfect, resulting in a non-functional device. Consequently, two other devices were manufactured using only silicon nitride as a substrate. This material, although not flexible, was chosen to ensure a completely electrically non-conductive substrate. While aluminum oxide was also considered as a substrate, the laboratory had mastered the silicone procedure the best, and there were time issues for introducing a new material.

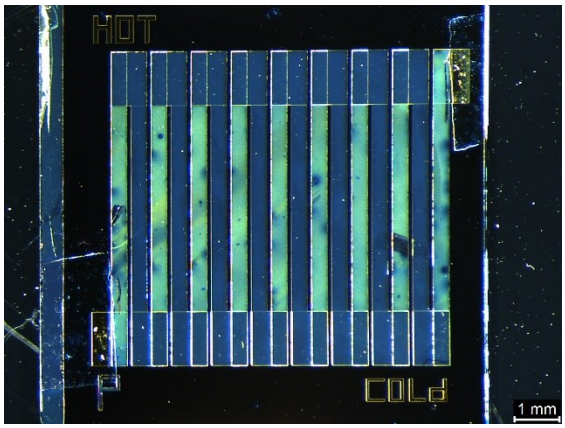

Figure 4-2: Leica LAS X microscope image of IFW TEG with silicon nitride on top.

Again, for laboratory simplicity, the dimensions were further reduced to a surface area of 1 cm x 1 cm. The two devices differ from each other only in that one of them has a thin silicon nitride layer on the top for protection and insulation (Figure 4-2). Both were found to be operational.

The materials used for the production are listed in the Table 1.

Table 1: IFW materials

Component	Material
n-type	Bismuth Telluride (Bi_2Te_3) 99.9999%
p-type	Antimony Telluride (Sb_2Te_3)
Connector	Gold (Au)

Production process

To sputter the thermoelectric materials and the gold, three masks (Figure 4-3) for each TEG were prepared by IFW workshop. The holes in the corners are for the correct alignment.

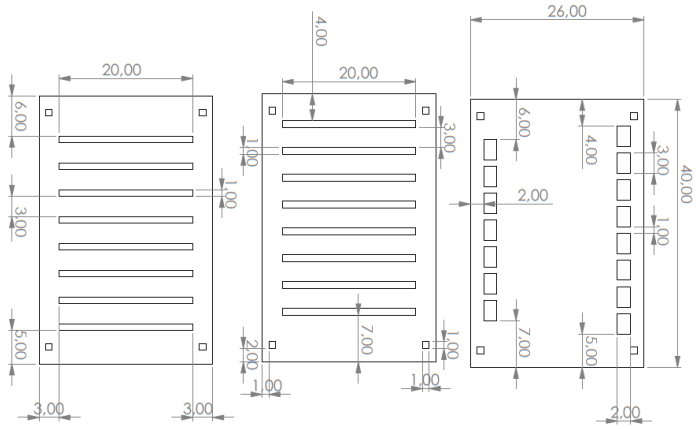

Figure 4-3: Masks for the first TEG (measures in mm)

The first material to be sputtered was Bismuth Telluride (Bi_2Te_3) with the following procedure and settings: 100 minutes for evacuating air from the chamber until reaching 10^{-3} Pa, then injecting argon with a flow of 55 SCCM (Standard Cubic Centimeters per Minute), followed by increasing the power to 50 W to ignite the plasma. Subsequently, the power was slowly decreased to 20 W and the vacuum level set at 7.5 E-7 Pa. Then, after a cleaning time of 40 minutes, the RF sputtering was started with a rate of 2 Å/s (0.2 nm/s).

The procedure was similar for Cu-doped Antimony Telluride (Sb_2Te_3)

Annealing

Since the entire sputtering procedure is carried out at ambient temperature, both thermoelectric materials result in a predominantly amorphous state with poor crystallinity and therefore low zT [41]. To improve the thermoelectric properties of the deposited films, post-annealing processes is required, even if it makes the materials brittle.

The annealing was performed in a quartz tube furnace (GSL-1100 K-LD) under high vacuum at 300°C for 4 h.

Material characteristics and devices characterization

The focus will be on the two smaller devices, since the first one did not work. The following data come from IFW laboratory.

Antimony Telluride has an electric conductivity of 44491 S/m (resistance 2.24765E-05 Ω) but of 90000 S/m (resistance 1.11111E-05 Ω) if it is Cu-doped, as in our case. Bismuth Telluride has an electric conductivity of 33353 S/m (resistance 2.99823E-05 Ω). The dimensions of the legs are: 2 cm x 1 mm. The thickness of the Sb_2Te_3 is 0.75 µm and 5 µm if Cu-doped, the one of the Bi_2Te_3 is 0.96 µm. The number of legs is 17. The Seebeck coefficient for Sb_2Te_3 is 112.56 µV/K and 80 µV/K if Cu-doped, the one of Bi_2Te_3 is -97.7 µV/K.

To evaluate the effective electrical resistance of the device, a current was applied on the TEGs and the voltage was measured. The results are in Table 2.

Table 2: I-V characterization

I (mA)	V (V)	R (Ω)
0.01	0.0445	4450
0.05	0.223	4460
0.1	0.4459	4459
0.2	0.8918	4459
0.3	1.3377	4459
0.4	1.7837	4459.25
0.5	2.2298	4459.6

The values were similar for the two devices. Considering the number of legs, the result was an average electric conductivity of 50096 S/m (resistance 1,99616E-05 Ω) and a Seebeck coefficient of 100 µV/K.

4.2.2 KIT TEG

The department of Printed Thermoelectric Devices of Karlsruhe Institute of Technology (KIT) collaborated in this thesis by providing 4 samples of customized printed thermoelectric generators.

Dimensions and materials

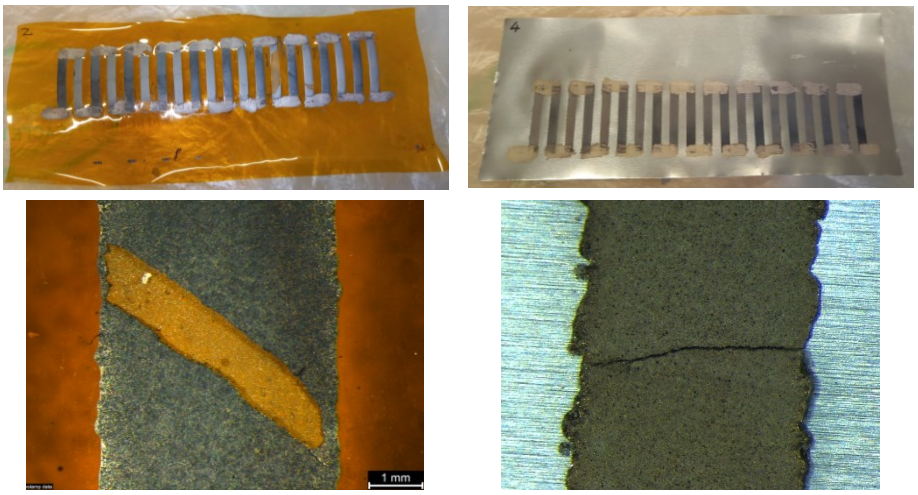

Figure 4-4: KIT TEG printed on Kapton (left) and on aluminum oxide (right). Below, examples of fracture are shown.

Using a semi-automated ROKUPRINT screen printing machine, KIT printed four TEGs, two on Polyimide and two on Aluminum oxide (Figure 4-4), and they were then annealed. As already mentioned, annealing is necessary but makes the materials brittle. The dimensions of the legs are approximately 3,5 cm x 0,5 cm. Unfortunately, due to the considerable length of the legs, many of them broke during transportation and delivery, but still, enough functioning legs in a row were found.

The materials of which these TEGs are made are listed in Table 3.

Table 3: KIT materials

Component	Material
n-type	$Bi_2Te_{2.7}Se_{0.3}$
p-type	$Bi_{0.5}Sb_{1.5}Te_3$
Connector	Silver (Ag)
Substrate A	Polyimide (PI)
Substrate B	Aluminum Oxide (Al_2O_3)

4.2.3 IPF TEG

The department of Functional Nanocomposites and Blends of the Leibniz Institute of Polymer Research (IPF) Dresden collaborated in this thesis by providing the two thermoelectric materials needed for the manufacture of a TEG.

Materials

These materials differ from the above mentioned because they are not metal alloy, but they are electrically conductive polymer composites (CPCs). This type of thermoelectric material is becoming subject of research due to the compromise provided by the relatively low thermal conductivity and high flexibility of the polymer component as well as the excellent power factor ($PF = S^2 \sigma$) of CNTs (carbon nanotubes) [42]. The ones used here are made with the solution mixing method.

Figure 4-5: p-type material on the left and n-type material on the right.

The p-type thermoelectric material is a thin circle of 9 cm diameter (Figure 4-5) with a Seebeck coefficient of around 52.32 μV/K. It is a combination of SWCNT (Single-Walled Carbon Nanotubes) 75% TUBALL and TPU (thermoplastic polyurethan) Estollan C85A10. It has an electrical conductivity of 27.82 S/m.

The n-type thermoelectric material is a thin circle of 5 cm diameter (Figure 4-5) with a Seebeck coefficient of -11.02 μV/K. It is a combination of nitrogen-doped MWCNT (multi-walled carbon nanotubes) 95% 30-50 micron and TPU. This film remained sticked on the filter paper. It has an electrical conductivity of 162.78 S/m.

Assembly

From the samples, two n-type legs and two p-type legs with dimensions of 0.5 cm x 2 cm were cut. A piece of aluminum tether was coated with Kapton tape to provide electrical insulation. The legs were then arranged on top of the tether, alternating between the two types, and secured in place using a bi-adhesive tape. Copper tape was used to connect the legs together (Figure 4-6), even though the recommended material to use was a conductive silver paste, which was unavailable at that time. This resulted in conductivity issues because both the thermoelectric materials and the adhesive of the copper tape have rough surfaces, leading to insufficient contact between the parts. The resistance was found to be impressively high, and therefore, the device was considered non-functional.

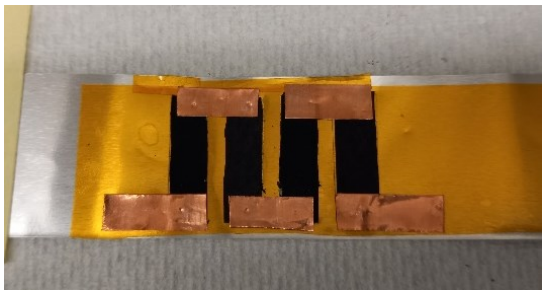

Figure 4-6: TEG created with IPF materials and copper tape.

4.3 Optical surfaces samples

TiNOX©

The company Almeco Group provided some samples of TiNOX© energy Cu, a highly selective blue coating for solar absorption with a copper substrate. From datasheet [43], it has a solar absorption (α) at 100°C of 95 % ± 2 % and a thermal emissivity (ε) at 100°C of 4 % ± 2 % that can also be seen in Figure 4-7. The chosen thickness was the minimum available: 0,12 mm.

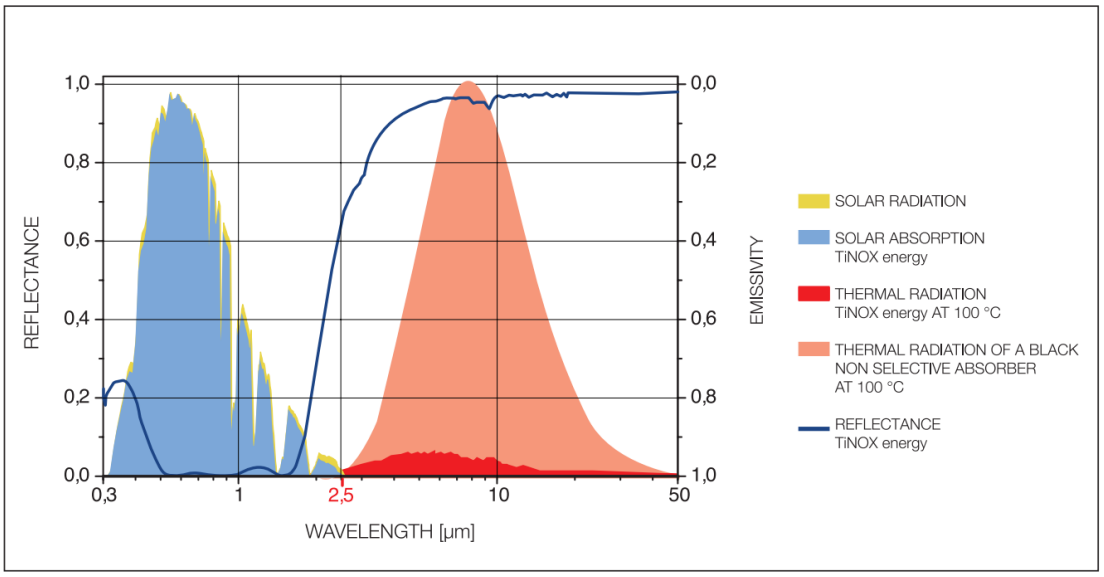

Figure 4-7: TiNOX reflectance spectrum. [43]

The material consists of 4 layers, as shown in Figure 4-8. The substrate material, copper, is a good thermal conductor and it is highly infrared-reflective. A diffusion barrier is applied to the adhesive layer. This prevents metal atoms from entering the absorber layer at high temperatures and changing the optical properties. This is followed by the absorber layer consisting of a multilayer cermet structure. Finally, the top layer is an anti-reflective, protective layer made of fused quartz.

This material is widely used on spacecrafts, for example to raise the temperature of a surface exposed to the sun [37].

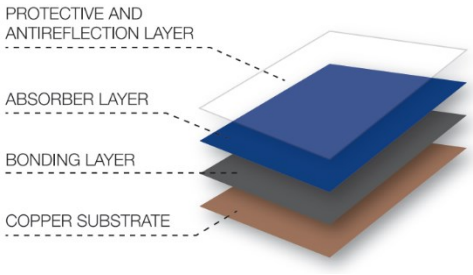

Figure 4-8: Layers that composes TiNOX material. [43]

Anodized aluminium

The company Steinert Anofol provided some samples of anodized aluminum. Since the thinner samples were only of 1 cm width, also thicker ones were taken into account. The types of samples are:

- BWALB 00459 AL99,5 0,050x10,00mm H18 hard (Oxide layer 4-5µm)
- BWALB 00059 AL99,5 0,100x125,00mm O soft (Oxide layer 5-6µm)

Anodized aluminum was chosen because it was already proposed for the flat-plate STEGs [20], [22] since it has high reflectance and high emissivity.

4.4 Instruments

Thermocouples

To measure temperature, thermocouples and a Measurement Computing's USB-TEMP device were utilized. Insulated twin twisted pair thermocouple cables of type K (Chromel-Alumel) were selected due to their commonality and temperature range of -50 to 250°C [44]. To connect the two cables, a Lampert PUK U4 welding machine was employed. Five of the thermocouples underwent calibration using freezing and boiling water in order to mitigate systematic errors. The behaviour of these five thermocouples was consistent, allowing for the assumption that the remaining thermocouples would exhibit similar behaviour.

The calibration results are presented in Table 4 and Table 5, where the uncertainty is calculated by multiplying the standard deviation by 2.26. This value comes from table [45] of the

t-distribution for a level of confidence of 95% and a number of degrees of freedom of n-1, n being the number of measurements (10).

Table 4: Calibration with boiling water: results and uncertainty calculation using t-student distribution.

	TC 1 [°C]	TC 2 [°C]	TC 3 [°C]	TC 4 [°C]	TC 5 [°C]
boil 1	98,3	98,6	98,65	98,59	98,47
boil 2	98,54	98,69	98,69	98,76	98,62
boil 3	98,62	98,7	98,89	98,97	98,11
boil 4	98,32	99,01	98,58	98,84	97,92
boil 5	98,2	98,4	98,75	98,77	98,96
boil 6	98,46	98,57	98,86	99,08	99,04
boil 7	98,55	98,61	98,9	99,13	99,16
boil 8	98,35	98,5	98,9	98,96	99,31
boil 9	98,37	98,45	98,89	98,99	99,04
boil 10	98,4	98,43	98,9	99,1	98,56
Average	98,411	98,596	98,801	98,919	98,719
Standard deviation	0,041189	0,056612	0,038771	0,055226	0,145842
Uncertainty (95%)	0,093088	0,127943	0,087623	0,12481	0,329603

Table 5: Calibration with melting ice: results and uncertainty calculation using t-student distribution.

	TC 1 [°C]	TC 2 [°C]	TC 3 [°C]	TC 4 [°C]	TC 5 [°C]
freeze 1	-0,3	-0,2	-0,13	-0,007	-0,66
freeze 2	-0,35	-0,3	0	-0,05	-0,6
freeze 3	-0,35	-0,22	-0,12	-0,06	-0,6
freeze 4	-0,3	-0,3	-0,05	0	-0,62
freeze 5	-0,32	-0,2	-0,1	0	-0,63
freeze 6	-0,32	-0,27	-0,04	0,02	-0,54
freeze 7	-0,28	-0,01	-0,13	0	-0,6
freeze 8	-0,25	-0,21	-0,02	-0,03	-0,5
freeze 9	-0,4	-0,24	-0,11	0,05	-0,57
freeze 10	-0,3	-0,23	-0,05	-0,04	-0,55
Average	-0,317	-0,218	-0,075	-0,0117	-0,587
Standard deviation	0,013254	0,025983	0,015293	0,010635	0,014985
Uncertainty (95%)	0,029954	0,058721	0,034563	0,024036	0,033867

The uncertainty was found to be low enough compared to the many other unknown factors that will be discussed later. However, during the boiling water measurements, the temperatures did

not reach 100°C due to difficulties in maintaining a constant boil with the type of boiler used for calibration. Nonetheless, the thermocouples are considered valid.

Solar simulator

The solar simulator (SoSi, Figure 4-9) was designed by Peiffer [12] to illuminate an area of 32 cm × 8 cm on a thermal plate at a distance of 10 cm inside the vacuum chamber. The light source is based on light emitting diodes (LEDs) and consist of four LED clusters, each consisting of 22 LEDs with 16 different peak wavelengths ranging from 270 nm to 1100 nm. Each cluster is surrounded by four square-shaped SEA-UV broadband surface mirrors with the intention of homogenizing and guiding the light. The LEDs are soldered to aluminum printed circuit boards (PCB) mounted on a liquid-cooled aluminum heat sink. [12]

Underneath the solar simulator, a cold plate can be placed, to simulate the cold of the space environment. It can be flushed with liquid nitrogen, that has a boiling temperature of -196°C [46].

Figure 4-9: Solar simulator.

Vacuum Chamber

The vacuum chamber has a diameter of 0.5 m and, in the actual condition, can reach a pressure of 10^{-5} mbar. It has different electrical and fluids interfaces. The pre-vacuum is created by a rotary vane backing pump that can bring the pressure under 1 mbar, then, the high vacuum is reached thanks to a turbomolecular pump.

The complete setup with the SoSi and the cold plate inside the vacuum chamber is shown in Figure 4-10.

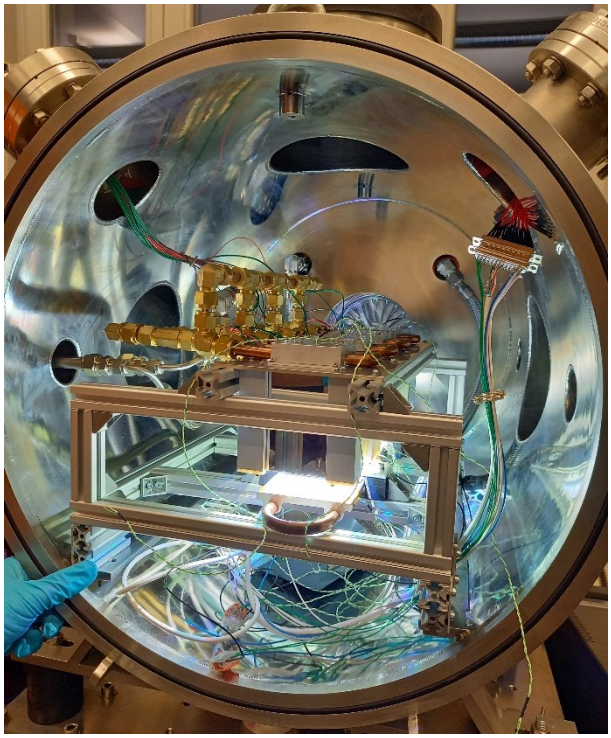

Figure 4-10: Solar simulator and cold plate in the vacuum chamber.

Source meter

The source meter used was a Keithley 2450 Source Measurement Unit (SMU). It was used to calculate the power of the TEGs. Some defined voltages were applied and the SMU measured the corresponding current, allowing to obtain the V-I characterization and therefore the power.

4.5 Setup and procedures

4.5.1 Setup

All the experiments were conducted at Institut für Luft- und Raumfahrttechnik (ILR) of the Technische Universität Dresden (TU Dresden).

Tests were conducted both in ambient air and in a vacuum chamber. In both cases, handles were required on which to place the tether. These handles served to maintain everything in position during movement and to ensure that the tether did not make contact with the cold plate underneath. Additionally, it was crucial to maintain the correct distance between the tether and the solar simulator to ensure the proper radiation energy.

The two handlers consist of two parts that can be screwed together to secure the tether (Figure 4-11). Furthermore, they can be attached to the base structure, where the solar simulator and the cold plate are also fixed. The lower parts were 3D printed in PLA (Polylactic acid) using PrusaSlicer, while the upper parts were crafted from aluminum to prevent outgassing issues at higher temperatures, as they are directly exposed to the solar simulator. Simulation using Ansys was conducted to ensure that the PLA components underneath would not become excessively hot.

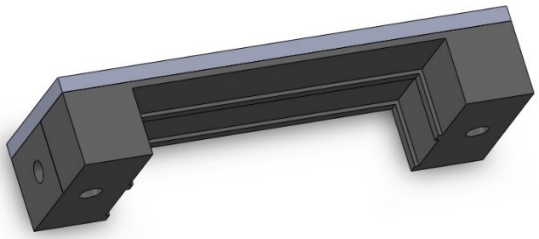

Figure 4-11: Holders to keep the sample in place designed with SolidWorks. The part in light grey is in aluminum, the other is in PLA.

4.5.2 Test of the optical surfaces

The initial experiments conducted aimed to assess whether the selective optical surfaces placed on a tether could indeed create a temperature gradient. These experiments took place in ambient air using the solar simulator. Pieces of aluminum tether measuring 2.5 cm x 7 cm were cut, and 1 cm wide strips of anodized aluminum on one side and TiNOX on the other were attached using a bi-adhesive, ensuring a distance of approximately 0.5 cm between the two strips. The same procedure was carried out using coated stainless steel instead of aluminum tether, as it was anticipated that some of the TEGs would be on stainless steel (Figure 4-12).

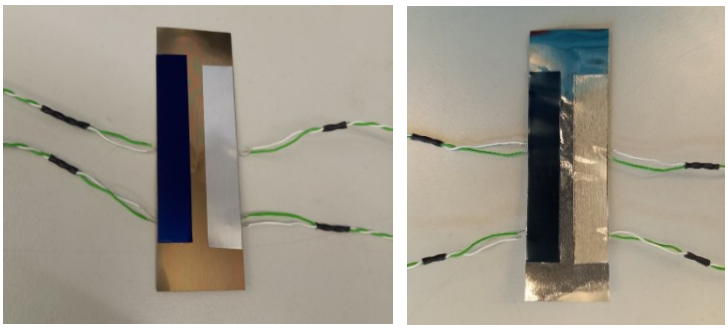

Figure 4-12: Samples to test the optical surfaces. Tether in stainless steel on the left and of aluminum on the right. The blue strip is TiNOX, the silver strip is anodized aluminum.

Four thermocouples were used, two on hot side and to on the cold side to also have a spatial information of the heating. Two tests for each tether material were run.

Results and analysis

The temperatures and temperature gradients reached are presented in Figure 4-13. In most cases, the two thermocouples on the same side show temperatures that differ by a couple of degrees. However, in all cases, both hot side temperatures are higher than both cold side temperatures, providing the initial evidence of the functionality of the selective optical surfaces and thus validating the concept.

The variance between temperatures on the same side is likely attributable to the challenge of maintaining the thermocouple in the correct position, as the adhesive used is not sufficiently strong. At times, the thermocouple remained attached only to the optical surfaces or only to the tether, rather than being in contact with both.

An important point to emphasize is that the temperature gradient for stainless steel is higher than that for aluminum, a fact easily explained by the thermal conductivity of the two materials. Aluminum exhibits very high conductivity, with a value of 237 $Wm^{-1}K^{-1}$ (Goodfellow Al 1200), while the conductivity of stainless steel is around 20 $Wm^{-1}K^{-1}$ [47].

The relatively low gradient and the rapid nullification of temperature gradients upon turning off the SoSi can be attributed to the ambient conditions in which the experiments were conducted. As previously mentioned, the experiments were not conducted in a vacuum, and therefore convection played a significant role in thermal transmissivity.

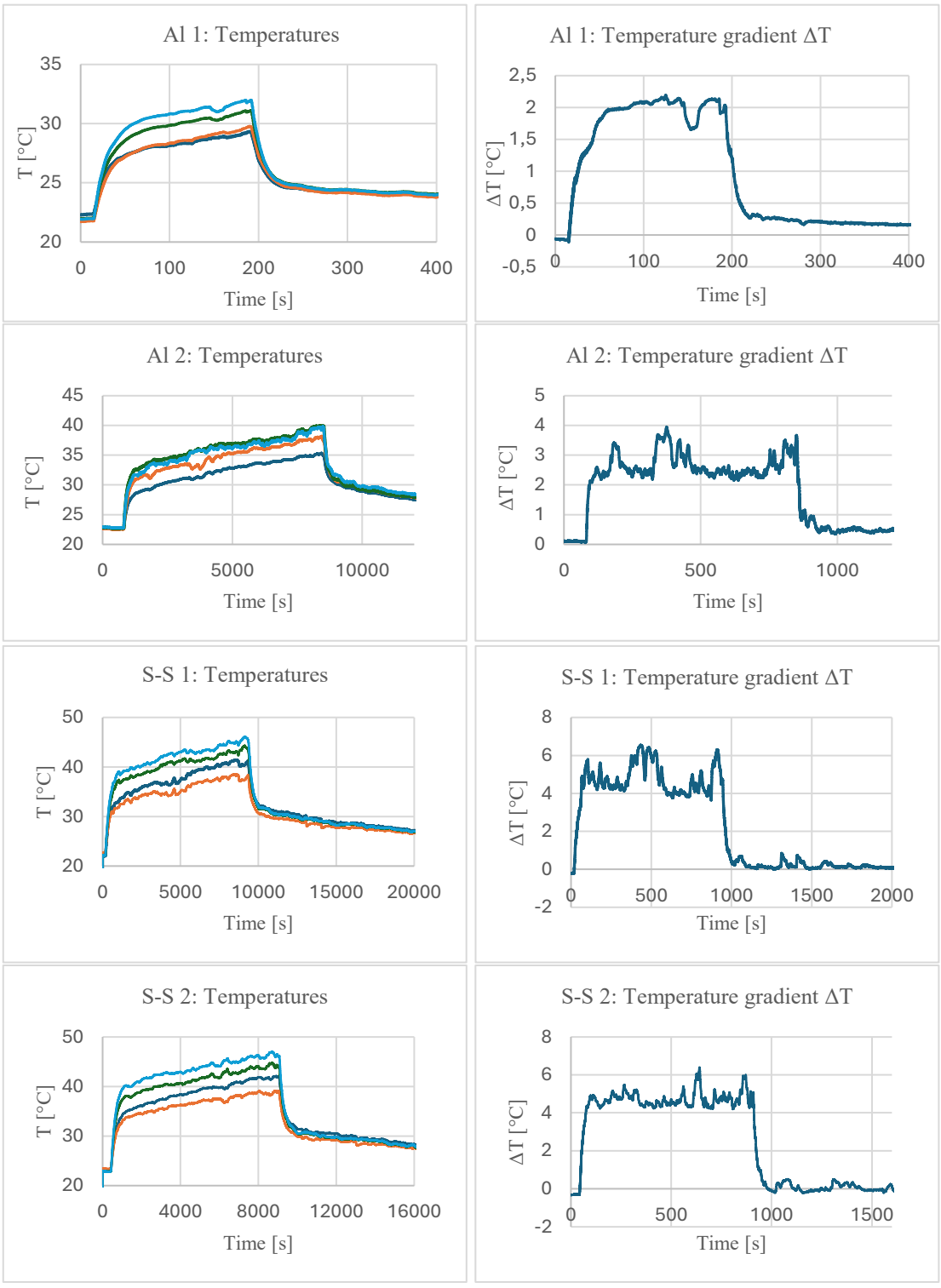

Figure 4-13: Results of the tests on the optical surfaces: on the left, there are the temperatures (green and light blue measured on the hot side, blue and orange on the cold side); on the right there are the gradients of temperature calculated using the average T.

4.5.3 Test of the KIT TEGs

The objective of these experiments was to evaluate whether the devices, with the application of optical surfaces, could generate power, and if so, to measure it. Prior to commencing the experiments, the parts of the devices that were more functional were identified, as some of the legs of the TEGs were broken. This assessment was conducted through visual observation and by measuring the resistance of each leg and connector using a multimeter. If the resistance was significantly higher compared to the others, it indicated that the leg or connector was likely broken.

Three out of the four samples were selected to undergo the experiments. From one aluminum sample, 12 legs with a total resistance of 164 Ω were identified (A). From one Kapton sample, 7 legs with a total resistance of 95 Ω were identified (B), and from the other Kapton sample, 11 legs with a total resistance of 3000 Ω were identified (C). The latter was primarily used to test the setup and obtain qualitative results, as the resistance was relatively high.

Once the sets of legs were selected, copper tape was applied to the first and last connector, and wires were soldered to the copper tape to establish the connection between the TEG and the SMU. Then, strips of anodized aluminum and TiNOX were affixed to the top of the opposite sides with bi-adhesive as shown in Figure 4-14. Thermocouples were inserted between the TEG and the optical surfaces to allow for correlation between the measured temperature gradient and the measured power.

During the assembly process, some legs deteriorated, therefore, the resistance of sample A went from 164 Ω to 267 Ω and the resistance of sample B from 95 Ω to 115 Ω. The average resistance of one leg is 22.25 Ω for sample A and 16.43 Ω for sample B.

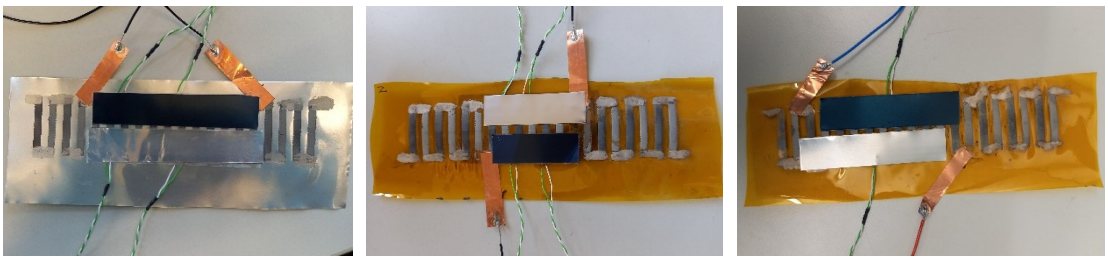

Figure 4-14: Assembly of the 3 KIT samples. From left to right: A, B, C.

Results and analysis

First, sample C was tested solely in ambient air to assess the possibility of generating power. The experiment was conducted twice: once with just the TEG on its Kapton substrate, and once with an aluminum tether underneath it. Kapton, being a poor thermal conductor unlike the real EDT setup, prompted the addition of aluminum to better simulate real conditions.

The results depicted in Figure 4-15 reveal that the presence of aluminum indeed altered the attainable temperature gradient: without aluminum, the ΔT was approximately 11 K, whereas with it, it decreased to around 5 K. Moreover, the power output was also impacted significantly: the maximum power point (MPP) without aluminum was 1.22E-08 W whereas, with aluminum, it dropped to 2.19E-09 W, almost 6 times lower.

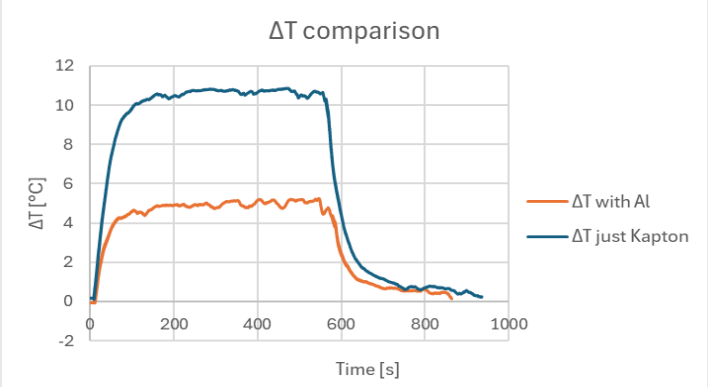

Figure 4-15: Comparison of gradient of temperature between the test with only Kapton and the test with aluminum substrate added underneath Kapton.

Afterwards, sample A, which has aluminum oxide as a substrate, was tested. The experiment conducted in ambient air yielded a temperature gradient of around 4ºC and a maximum power point of 7.15E-09 W. This result is reasonable because the gradient is similar to the one achieved with sample C with aluminum, but the power output is higher because sample A is more performant.

The same experiment was then conducted in a vacuum, where the temperatures and the gradients were significantly higher than in the previous experiment. At its maximum, the temperature of the hot plate was almost 110ºC, the gradient was around 28ºC, and the maximum

power point was 3.82E-08 W. Figure 4-16 and Figure 4-17 depict the trends of temperatures, gradients, and power.

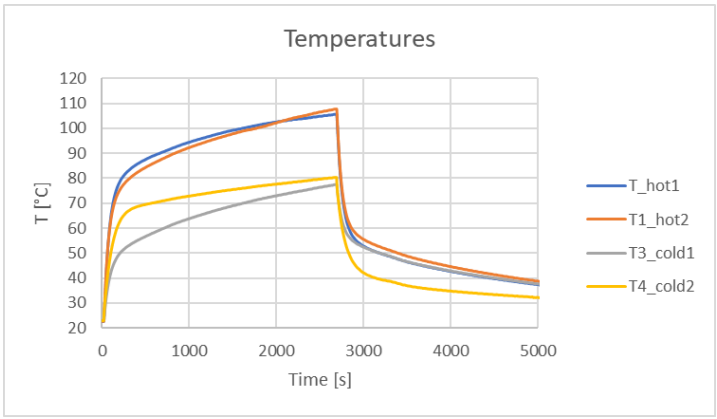

Figure 4-16: Sample A in vacuum: temperatures.

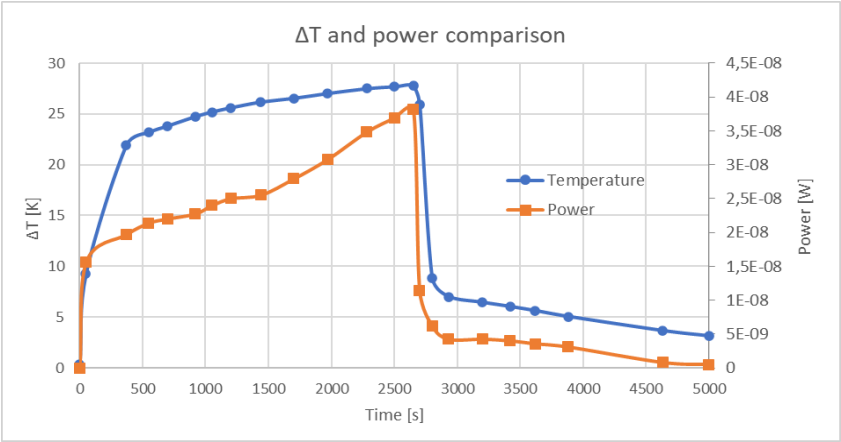

Figure 4-17: Sample A in vacuum: comparison between the trend of the T gradient and the trend of the maximum power point during the experiment.

Also in a vacuum, but with the cold plate cooled with liquid nitrogen, the third experiment on sample A was conducted. This was done to assess whether the presence of a cooling plate would yield consistent differences in the results. The maximum power point was 2.92E-08 W. Both temperature and I-V trends were sufficiently similar to decide against using the cold plate again, especially considering the difficulties associated with using a substance as liquid nitrogen.

The last KIT TEG tested was sample B, which has Kapton as a substrate, but a tether of stainless steel coated with aluminum oxide was placed underneath to better simulate the real situation. It was tested in both ambient air and vacuum conditions. Unfortunately, during the experiment

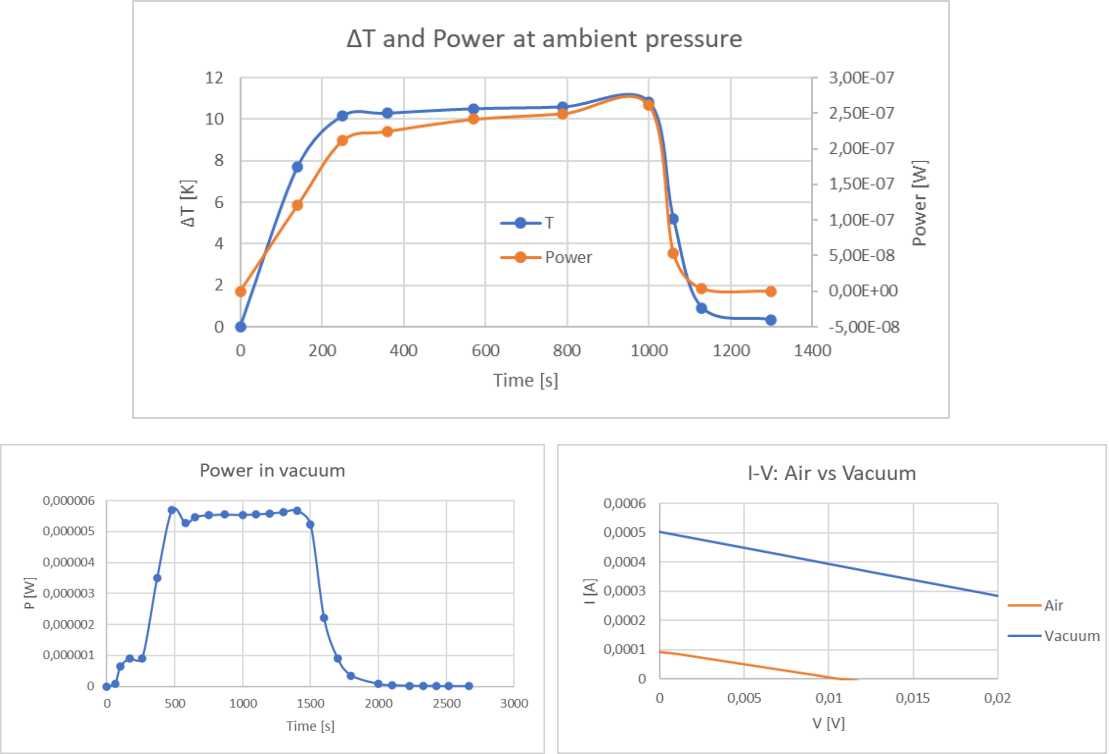

Figure 4-18: Sample B graphics: on the top there is the comparison between the trends of temperature and MPP during the experiment in ambient air; on the bottom left there is the MPP trend during the experiment in vacuum; on the bottom right there is the comparison between I-V curves in air and in vacuum.

in vacuum, all the thermocouples completely detached from the sample, rendering no information about the temperatures available. It was decided not to repeat the test, as it was likely that the same problem would occur again, especially considering the high temperatures reached. The issue of surfaces and thermocouples detaching is further discussed in the following chapters.

The results are reported in Figure 4-18. In ambient air, the highest temperature was around 50ºC, the maximum temperature gradient around 11 K, and the maximum power point 2.62E-07 W. Instead, in vacuum, the maximum power point was 5,70E-06 W, significantly higher than in air. The difference in power can easily be seen also looking at the I-V data collected in the two tests (Figure 4-18 on the bottom right).

4.5.4 Test of the IFW TEG

For these experiments, the setup was more challenging due to the reduced dimensions of the TEGs. Only one IFW device was tested, as one was non-functional, and another was reserved for characterization by IFW. The selected device for testing was the one with silicon nitride on top, as it was considered to offer better protection and thus be easier to use. The sample was placed on a stainless steel tether, both to better simulate the metallic material of the real setup and for ease of use with the setup used for KIT TEGs.

Initially, the same copper tape setup soldered with wires was attempted, but it resulted in very high resistance when measured both with a multimeter and the SMU. It is likely that for a device of these dimensions, with connectors less than a millimeter in size, the copper tape had insufficient contact area with the connectors, considering that the adhesive of the tape was relatively rough. The solution was to directly use alligator clips on the connectors as shown in Figure 4-19.

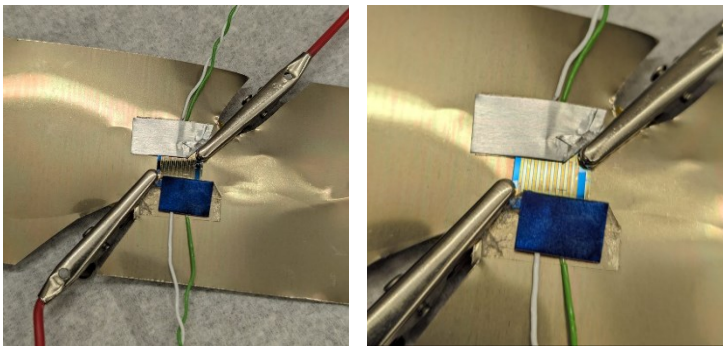

Figure 4-19: Assembly of the IFW sample.

Results and analysis

The sample was initially tested in ambient air and then in vacuum. Similar to previous occurrences, the thermocouples encountered issues during the vacuum experiment, resulting in temperature information being available only for the first test. As depicted in Figure 4-21, the highest temperature was around 46ºC and the gradient around 2 K, which is lower than that observed for the KIT TEGs.

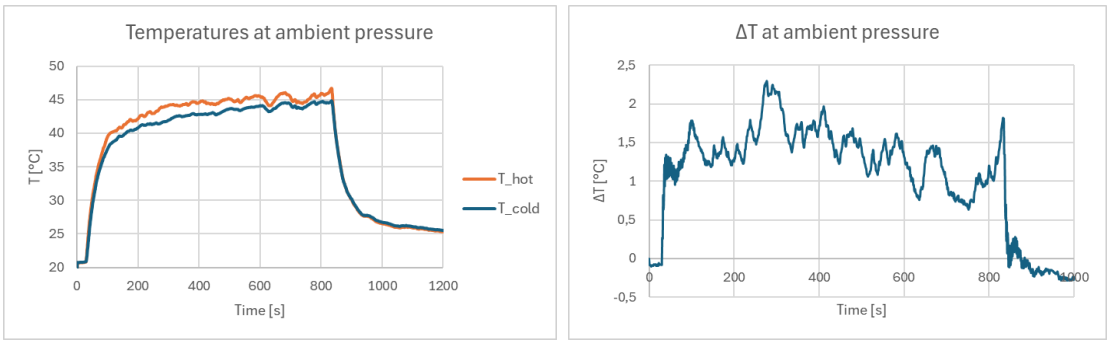

Figure 4-21: Temperatures results for ambient air experiment.

At its highest, the maximum power point in ambient air was 7.26E-13 W and in vacuum 3.67E-13 W, much lower than in KIT TEGs. As reported in Figure 4-20, the power in ambient air is slightly higher than in vacuum and the trend of the maximum power point during the experiment is not as expected, as it fluctuates instead of remaining stable.

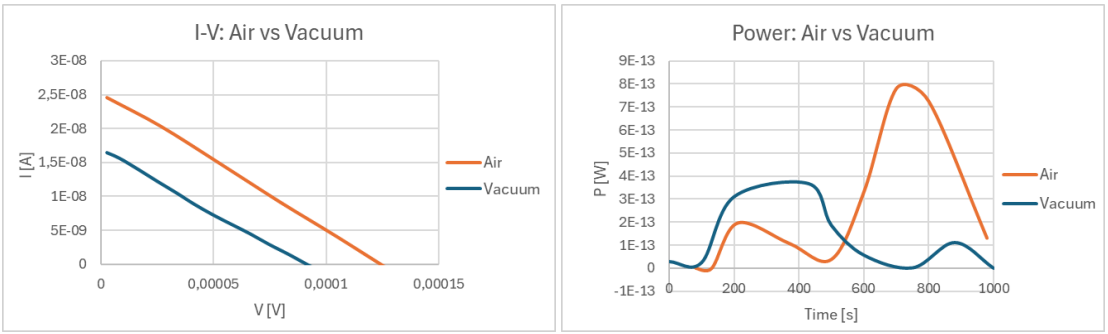

Figure 4-20: Comparison between IFW TEG in vacuum and in ambient air.

4.5.5 Atomic Oxygen experiment

As previously explained, atomic oxygen can pose a problem in LEO environments. The ILR of TU Dresden has atomic oxygen exposure facility (ATOX) (Figure 4-22); atomic oxygen is generated in a microwave-based low-pressure oxygen plasma and released into a vacuum chamber, creating a flow of atomic oxygen and other gaseous species to a sample. The non-functioning IFW sample was tested in it to ensure that none of the functional TEGs were damaged. The flux density of atomic oxygen measured in the worst case corresponds to $\Phi = (2{,}43 \pm 0{,}92)\ 10^{14}\ \frac{atoms}{cm^2\ s}$. The test stand was on for 24 h and 3 min, resulting in a fluence of atomic oxygen of at least $F = (2{,}10 \pm 0{,}80) \times 10^{19}\ \frac{atoms}{cm^2}$.

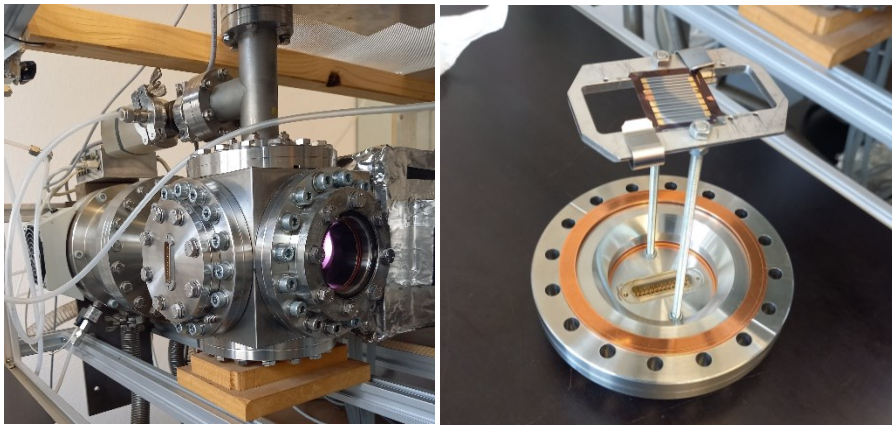

Figure 4-22: Atomic oxygen machine on the left, positioning of the TEG on the right.

Results

The results are evaluated qualitatively by observing the sample before and after exposure. It is evident that one type of leg, particularly those made of bismuth telluride, underwent a change in colour, becoming darker (Figure 4-23). From literature, these two materials have indeed a difference in oxidation [48].

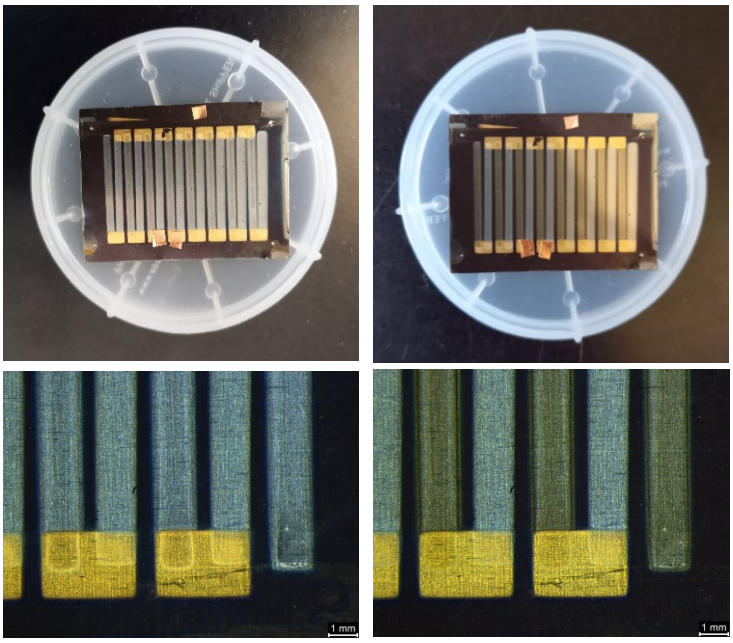

Figure 4-23: TEG before (right) and after (left) atomic oxygen exposure. The pictures on the bottom are taken with Leica LAS X microscope.

4.6 Summary and discussion of experiments results

Table 6: summary of results.

Name	Substrates	N. legs	ΔT [K]	MPP [W]	MPP/m [mW/m]	MPP/m² [mW/m²]
KIT C1	Kapton	11	11	1,22E-08	1,11E-04	3,17E-03
KIT C2	Kapton & Al	11	5	2,19E-09	1,99E-05	5,69E-04
KIT A air	Al oxide	12	4	7,15E-09	5,96E-05	1,70E-03
KIT A vac	Al oxide	12	28	3,82E-08	3,18E-04	9,10E-03
KIT B air	Kapton & S-S	7	11	2,62E-07	3,74E-03	1,07E-01
KIT B vac	Kapton & S-S	7	N.D	5,70E-06	8,14E-02	2,33E+00
IFW air	Silicon nitride	17	2	7,26E-13	7,26E-08	7,26E-06
IFW vac	Silicon nitride	17	N.D	3,67E-13	3,67E-08	3,67E-06

Table 6 summarizes all the numeric results of the experiments with also the calculation of the power per unit of length (MPP/m) and the surface power density (MPP/m^2). The best-performing TEG is sample B from KIT, which with just 7 legs, achieved the highest MPP, the highest MPP/m and the highest MPP/m^2, that is in the order of milliwatt/m. Comparing it with the other experiments, it is probable that the temperature gradient was around 50 K. This result was anticipated, as the average electrical resistance of the legs was the lowest, and Kapton, being a poor thermal conductor, allows for a greater temperature gradient between the two sides of the TEG. Although the stainless steel (S-S) substrate underneath it brings it closer to the real situation, S-S is still much less thermally conductive than the actual aluminum tether.

In all KIT TEGs, experiments conducted in vacuum resulted in higher temperature gradients and consequently higher powers. This outcome was expected because in vacuum there is no convection, and heat transfer is dominated by conduction and emissivity. To assess whether convection could be ignored in the ILR vacuum chamber, the Knudsen number was calculated, resulting in over 2000 at the pressure of 10^{-5} mbar, the pressure used during the tests. Since the number exceeds 10, the regime can be considered a free molecular regime [49], indicating the absence of convection and air conduction [50].

Upon examining the results and observing the samples after the experiments, the main problem encountered was the detachment of the thermocouples and the optical surfaces from the TEGs. Among the two selective optical surfaces, TiNOX was significantly more affected by this problem due to its rigidity and higher temperatures (Figure 4-24). The elevated temperatures not only reduced the effectiveness of the adhesive but also led to differential expansion in each material, complicating the adhesion problems.

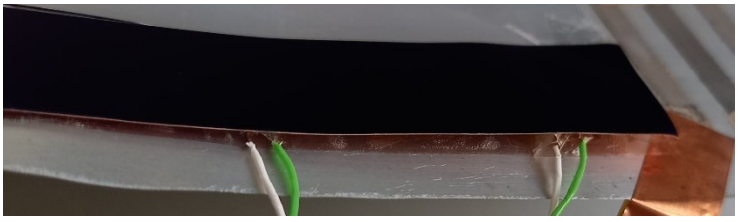

Figure 4-24: Detachment of TiNOX from the TEG.

IFW TEGs exhibited lower power results than all the KIT samples. The reasons for this can be attributed not to the effective efficiency of the device, but rather to its dimensions, which were difficult to handle with the available instruments. For instance, the thermocouples occupied a

significant portion of the surface of the TEG, hindering the contact between the optical surfaces and the device. With this consideration, it is possible to explain why the power trend during the experiment was so fluctuant: initially, everything was correctly positioned, leading to an increase in power with temperature, but as the experiment progressed, the surfaces detached, and the desired effect of the optical selective surfaces diminished.

The final observation pertains to the temperature gradients observed after the SoSi is deactivated. In vacuum conditions, the temperature decreases at a slower rate compared to ambient air, and it takes a couple of minutes for the gradient to reach zero. This phenomenon is also reflected in the power output, which decreases more gradually in vacuum than in ambient air. However, the gradient after deactivation is lower than anticipated. This discrepancy may be attributed once again to the detachment of the surfaces and the thermocouples.

5. Simulations

5.1 Objectives

The objective of the simulations was to gain an understanding of the temperatures and gradients achievable. This was crucial for assessing the feasibility of the concept and determining whether it was worthwhile to proceed with laboratory experiments. Additionally, they played a crucial role in discussions with institutes to secure samples and materials, as they provided data on the expected temperature gradients. Finally, understanding the temperature range was important in selecting thermoelectric materials, as each material has temperatures of optimal efficiency.

Most of the simulations were conducted using Ansys Mechanical, which is a finite element analysis (FEA) software. The specific module utilized was Steady State Thermal Analysis.

5.2 Methods

The initial simulations focused solely on the tether and the optical surfaces. A 3D model consisting of a 7 cm long and 2.5 cm wide piece of tether, along with one strip of TiNOX and one of anodized aluminum, was designed and assembled using SolidWorks. Subsequently, the model was imported into Ansys Mechanical. The material characteristics that were input into the software are listed in table.

Table 7: Thermal conductivity (λ), emissivity (ε) and absorbance (α) of the materials used in the simulations.

Material	λ [W/m·K]	ε	α
Aluminum Tether	237	0.09	0.03
Anodized Al	200	0.9	0.14
TiNOX	320	0.04	0.9

The ambient temperature was maintained at 3 K to simulate the space environment. The solar flux was simulated by applying a heat flux to each front surface, with an intensity calculated by multiplying the solar constant at AM0 (1367 W/m^2) by the absorption coefficient (α). This approach was necessary because Ansys Mechanical treats absorption and emissivity as equivalent [51], making it impossible to directly simulate a solar flux and set the α values separately.

To emphasize the importance of the thermal conductivity of the substrate, the same simulation was conducted by altering this value, reducing it compared to the one of aluminum.

Since, as previously mentioned, the orientation of the tether varies due to orbit and twisting, another simulation was conducted with the sun positioned on the opposite side of the tether. In this scenario, the solar radiation shines on the backside of the tether, where the only visible object is the tether itself. Consequently, the absorption coefficients of the optical surfaces become irrelevant, and the focus shifts to the effect of the different emissivity between TiNOX and anodized aluminum.

Some additional simulations were performed in an attempt to replicate the thermoelectric generators and the experimental setup using SolidWorks and Ansys. However, a significant

challenge was encountered in replicating the TEGs accurately in CAD due to the thin and flexible nature of the materials used. Furthermore, given that most of the TEG's surface is covered by optical surfaces and thermoelectric materials typically exhibit low thermal conductivity between the hot and cold plates, simulating the entire device was considered redundant.

5.3 Results and conclusions of the simulations

In Figure 5-1, the steady-state temperatures reached by the aluminum and the optical surfaces when the sun is on the front are visually represented, demonstrating the creation of a temperature gradient. The highest temperature on the object is 426.93 K (153.78 °C), and the gradient between the hot and the cold side is 7.86 K, theoretically sufficient to generate measurable power when applied to a TEG.

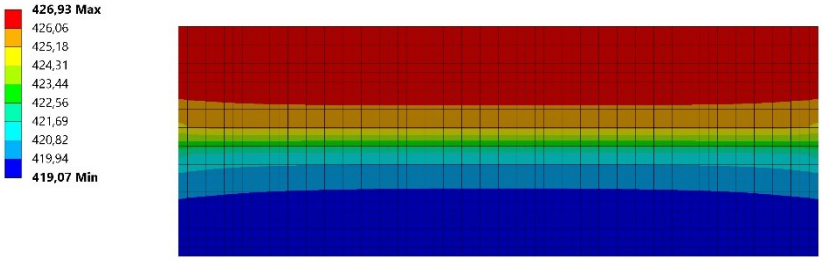

Figure 5-1: Ansys thermal simulation of Al and optical selective surfaces when the sun in on the front. Temperatures are in Kelvin.

Conversely, when the sun is on the back, the highest temperature on the object is 341.78 K (68.63°C), and the gradient is 2.16 K. The generally lower temperatures are attributed to the fact that the aluminum of the tether itself acts as a reflector, absorbing less solar radiation. The lower gradient is instead due to the fact that it is created only by the difference in emittance between TiNOX and anodized aluminum, not by the difference in absorbance. However, the fact that the gradient is above zero suggests that the device will be able to generate power in any conditions.

Figure 5-2 illustrates a comparison of temperatures when changing the thermal conductivity of the substrate from aluminum to something less conductive. As previously stated, with a thermal conductivity of 237 W/m·K (equivalent to that of aluminum), the gradient is 7.86 K. With a

conductivity of 150 W/m·K, the gradient increases to 10.28 K, while with a conductivity of 100 W/m·K, it further rises to 13.54 K. Finally, with a conductivity of 50 W/m·K, the gradient reaches 22.46 K. Thus, it is evident that the gradient significantly increases when the substrate's conductivity decreases.

Given that the E.T.Pack tether is in aluminum and cannot be modified, attention is directed toward the material on which the TEG will be printed or sputtered. This material will need to serve also as a thermal insulator.

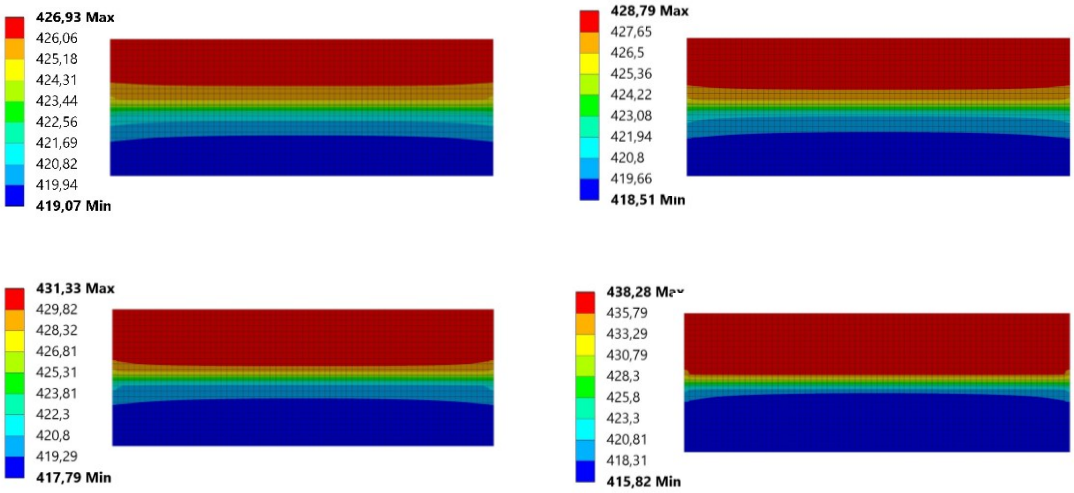

Figure 5-2: Ansys thermal simulations changing the thermal conductivity of the substrate. 237 W/m·K top left, 150 W/m·K top right, 100 W/m·K bottom left, 50 W/m·K bottom right.

6. Conclusions and Outlook

The aim of this study was to assess the feasibility of placing a solar-enhanced thermoelectric generator (TEG) on the surface of an electrodynamic tether. The design process prioritized meeting all requirements for thickness, flexibility, and suitability for the space environment. Consequently, a planar configuration was chosen. To create a temperature difference between the hot and cold plates, materials with specific optical selectivity were identified: TiNOX as the absorber and anodized aluminum as the reflector.

Simulations and experiments confirmed the feasibility of power generation using the chosen design. This was achieved with a variety of TEGs received from or assembled with three major German institutes.

Observations regarding the results of this thesis are necessary for comparison with other options and to evaluate the merit of continuing research in this direction.

Comparison between simulations and experiments

In terms of temperature gradient, there is agreement between simulations and experiments. The tests conducted on stainless steel with the two strips of optical surfaces yielded a ΔT of about 4 K, while the simulation of the same setup resulted in a ΔT of about 7 K, but in vacuum, where higher gradient is expected. Despite the inherent challenges of experimentation, the results demonstrate a consistent correspondence.

Comparison with TEG state of the art in terms of power

During the review of state-of-the-art thin, flexible thermoelectric generators, it was found that they typically exhibit power densities ranging from of 0.1 to 100 mW/m^2, with temperature gradients between 50 and 150 K. The best-performing sample, in the experiments here presented, achieved a maximum power point of 5.70E-06 W in vacuum, corresponding to a power density of 2.33 mW/m^2, with a temperature gradient that was likely around 50 K. This result aligns well with existing research in the field. The sample in question was manufactured by screen printing BiTe and SbTe on a thin flexible Kapton substrate, that was then placed on a piece of stainless steel to emulate the tether. While Kapton has a long history of space use,

further considerations are needed for BiTe and SbTe, particularly regarding their susceptibility to atomic oxygen degradation, even if they have both already been used for space applications. In fact, the ATOX experiment conducted during this work was just qualitative.

Evaluation of power for E.T.Pack

Considering the E.T.Pack project, the power density of 2.33 mW/m^2 is relatively low. To achieve 1 W of power, almost 17 km of tether would be required. Additionally, it's important to consider the effects of solar radiation angle and tether twisting in orbit. In reality, the angle of the sun's rays on the tether would constantly change, and the tether would be subject to periods of complete shadow. Moreover, due to the deployment mechanism, the tether will be twisted, so every portion of it will receive solar radiation with a different angle. Although this aspect was only marginally evaluated in the presented work, it's evident that accounting for these factors would significantly decrease the power output of the TEG.

Comparison with solar cells

It is also important to compare the results of this study with those obtained from the integration of solar cells onto the EDT. While the experimentally measured power from the TEGs is lower than that from solar cells, the advantage lies in the ability to generate a voltage difference even when not directly exposed to sunlight. This was demonstrated both through simulations and experiments, highlighting a potential advantage of TEGs over solar cells in certain scenarios.

Flexibility

Even though, theoretically, all the devices were supposed to be flexible, not all of them turned out to be so. The TEGs from IFW were sputtered onto silicon nitride, which is not flexible. Similarly, the TEGs from KIT, although printed on flexible materials, were not truly flexible, as many of the thermoelectric legs broke during handling. This was mainly due to the properties of the materials BiTe and SbTe, which show only limited flexibility, especially after annealing. Flexibility, as considered in the state of the art, is primarily focused on the substrate rather than along the legs, which is why they claim to have flexible devices. However, since flexibility along the length of the tether is indeed crucial, rather than along the width, it is likely that the thermoelectric materials themselves will not pose significant issues.

It is important to note that the IPF TEG was the only one with consistent flexibility in all directions, as it was made from completely different materials (CPCs). Unfortunately, no power performance could be measured for this TEG due to the impossibility of obtaining the right connector paste within a useful timeframe.

Outlook

Firstly, is it crucial to find an alternative to copper tape for better wire connection to the TEGs and for connecting the legs of the IPF TEGs together. Additionally, a stronger adhesive that can withstand high temperatures should be identified and utilized to attach the optical surfaces to the TEGs and to properly insert the thermocouples for temperature measurement.

To address the issue of fragile legs, one approach could be to shorten their length. This would allow for the placement of two different TEGs side by side, working in parallel while still utilizing the full width of the tether (Figure 6-1).

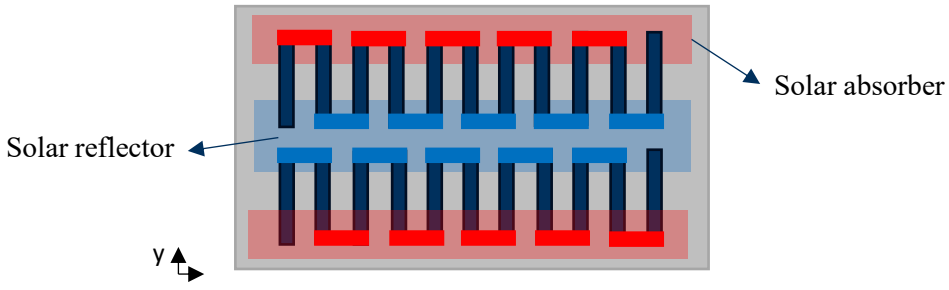

Figure 6-1: Two strips of TEGs on the tether: future evaluation.

Furthermore, to better assess the real-world application within the E.T.Pack project, a deeper investigation into the twisting problem is necessary. This involves creating a function to express the intensity of solar radiation across each part of the twisted tether and establishing a setup that allows for the twisting of samples during experiments. Additionally, a study on the electrical connection with the rest of the E.T.Pack systems is essential for evaluating practical applicability.

Given the results and studies conducted thus far, it appears that placing thermoelectric generators on the EDT may not provide sufficient power assistance to be considered useful and worthwhile. However, since the concept analyzed in this thesis has been demonstrated to be functional, ongoing research on planar TEGs for satellite applications could yield significant results and applications in the future.

References

[1] ESA, “ESA Space Debris Mitigation Requirements,” *ESA UNCLASSIFIED*. 2023. doi: ESSB-ST-U-007 Issue 1.

[2] IADC, “IADC Space Debris Mitigation Guidelines,” *IADC Action Item number 22.4*. 2007.

[3] NASA, “Deorbit Systems,” 2022. Accessed: Dec. 26, 2023. [Online]. Available: https://www.nasa.gov/smallsat-institute/sst-soa/deorbit-systems/

[4] “The E.T.PACK Initiative.” Accessed: Dec. 29, 2023. [Online]. Available: https://etpack.eu/

[5] G. Sánchez-Arriaga *et al.*, “The E.T.PACK project: Towards a fully passive and consumable-less deorbit kit based on low-work-function tether technology,” *Acta Astronaut*, Dec. 2020, doi: 10.1016/J.ACTAASTRO.2020.03.036.

[6] L. Tarabini Castellani *et al.*, “Deorbit kit demonstration mission,” *Journal of Space Safety Engineering*, vol. 9, no. 2, pp. 165–173, Jun. 2022, doi: 10.1016/j.jsse.2022.01.004.

[7] M. Tajmar and G. Sánchez-Arriaga, “A bare-photovoltaic tether for consumable-less and autonomous space propulsion and power generation,” *Acta Astronaut*, Mar. 2021, doi: 10.1016/j.actaastro.2020.12.053.

[8] S. B. Khan and J. R. Sanmartin, “Survival probability of round and tape tethers against debris impact,” *J Spacecr Rockets*, 2013, doi: 10.2514/1.A32383.

[9] G. Sánchez-Arriaga and J. R. Sanmartín, “Electrical model and optimal design scheme for low work-function tethers in thrust mode,” *Aerosp Sci Technol*, Jan. 2020, doi: 10.1016/j.ast.2019.105519.

[10] G. Sarego *et al.*, “Deployment requirements for deorbiting electrodynamic tether technology,” *CEAS Space Journal*, Oct. 2021, doi: 10.1007/s12567-021-00349-5.

[11] G. Sarego *et al.*, “Deorbiting Performance of Electrodynamic Tethers to Mitigate Space Debris,” *World Academy of Science, Engineering and Technology International Journal of Aerospace and Mechanical Engineering*, 2021.

[12] L. Peiffer, C. Perfler, and M. Tajmar, “Feasibility Study of the Bare-Photovoltaic-Tether Concept: Prototypes and Experimental Performance Evaluation of the Photovoltaic Tether Segment,” *Aerospace*, Apr. 2023, doi: 10.3390/aerospace10040386.

[13] J. R. Sanmartín, E. C. Lorenzini, and M. Martinez-Sanchez, “A Review of Electrodynamic Tethers for Space Applications,” in *AIAA*, 2008. doi: https://doi.org/10.2514/6.2008-4595.

[14] D. Enescu, “Thermoelectric Energy Harvesting: Basic Principles and Applications,” in *Green Energy Advances*, IntechOpen, 2019. doi: 10.5772/intechopen.83495.

[15] M. von Lukowicz, E. Abbe, T. Schmiel, and M. Tajmar, “Thermoelectric Generators on Satellites—An Approach for Waste Heat Recovery in Space,” *Energies (Basel)*, Jul. 2016, doi: 10.3390/en9070541.

[16] Q. Zhang, K. Deng, L. Wilkens, H. Reith, and K. Nielsch, “Micro-thermoelectric devices,” *Nature Electronics*. Nature Research, Jun. 01, 2022. doi: 10.1038/s41928-022-00776-0.

[17] G. R. Schmidt, T. J. Sutliff, and L. A. Dudzinski, “Radioisotope Power: A Key Technology for Deep Space Exploration,” in *Radioisotopes - Applications in Physical Sciences*, 2011. [Online]. Available: www.intechopen.com

[18] D. Payne, “Thermal analysis and designs for non-radioactive thermoelectric generators for common small satellite types,” BOSTON UNIVERSITY, 2020. [Online]. Available: http://open.bu.edu

[19] M. Telkes, “Solar Thermoelectric Generators,” *NASA Center for Aerospace Information*. 1954. doi: NASA-CR-157C97.

[20] N. Fuschillo, R. Gibson, P. K. Eggleston, and J. Epstein, “Solar Thermoelectric Generator for Near-Earth Space Applications,” *IEEE* , 1962.

[21] D. Kraemer *et al.*, “High-performance flat-panel solar thermoelectric generators with high thermal concentration,” *Nat Mater*, 2011, doi: 10.1038/nmat3013.

[22] L. Liu, X. Sen Lu, M. L. Shi, Y. K. Ma, and J. Y. Shi, “Modeling of flat-plate solar thermoelectric generators for space applications,” *Solar Energy*, Jul. 2016, doi: 10.1016/j.solener.2016.03.028.

[23] E. M. F. Vieira *et al.*, “High-Performance μ-Thermoelectric Device Based on Bi2Te3/Sb2Te3 p-n Junctions,” *ACS Appl Mater Interfaces*, Oct. 2019, doi: 10.1021/acsami.9b13254.

[24] K. Kato, Y. Hatasako, M. Kashiwagi, H. Hagino, C. Adachi, and K. Miyazaki, “Fabrication of a flexible bismuth telluride power generation module using microporous polyimide films as substrates,” *J Electron Mater*, Jun. 2014, doi: 10.1007/s11664-013-2852-0.

[25] V. Karthikeyan *et al.*, “Wearable and flexible thin film thermoelectric module for multi-scale energy harvesting,” *J Power Sources*, Apr. 2020, doi: 10.1016/j.jpowsour.2020.227983.

[26] S. Hou *et al.*, “High-performance, thin-film thermoelectric generator with self-healing ability for body-heat harvesting,” *Cell Rep Phys Sci*, Nov. 2022, doi: 10.1016/j.xcrp.2022.101146.

[27] Y. Liu *et al.*, “High performance Ag2Se films by a one-pot method for a flexible thermoelectric generator,” *J Mater Chem A Mater*, Nov. 2022, doi: 10.1039/d2ta07892a.

[28] D. L. Wen, H. T. Deng, X. Liu, G. K. Li, X. R. Zhang, and X. S. Zhang, “Wearable multi-sensing double-chain thermoelectric generator,” *Microsyst Nanoeng*, Dec. 2020, doi: 10.1038/s41378-020-0179-6.

[29] T. Nguyen Huu, T. Nguyen Van, and O. Takahito, “Flexible thermoelectric power generator with Y-type structure using electrochemical deposition process,” *Appl Energy*, Jan. 2018, doi: 10.1016/J.APENERGY.2017.05.005.

[30] J. Zang *et al.*, “Printed flexible thermoelectric materials and devices,” *J Mater Chem A Mater*, Sep. 2021, doi: 10.1039/d1ta03647e.

[31] M. S. Hossain, T. Li, Y. Yu, J. Yong, J. H. Bahk, and E. Skafidas, “Recent advances in printable thermoelectric devices: Materials, printing techniques, and applications,” *RSC Advances*. Royal Society of Chemistry, Feb. 26, 2020. doi: 10.1039/c9ra09801a.

[32] “Magnetron Sputtering: Overview,” Angstrom Engineering. Accessed: Jan. 21, 2024. [Online]. Available: https://angstromengineering.com/tech/magnetron-sputtering/

[33] Matt Hughes, “What is RF Sputtering?,” Semicore. Accessed: Jan. 28, 2024. [Online]. Available: https://www.semicore.com/news/92-what-is-rf-sputtering

[34] F. Miglietta, “Trasmissione del calore per irraggiamento,” in *Elementi di Fisica Tecnica*, 2017.

[35] NASA, “Infrared Waves,” Science Mission Directorate. Accessed: Feb. 04, 2024. [Online]. Available: https://science.nasa.gov/ems/07_infraredwaves

[36] David Thorpe, “Emissivity and absorption of materials,” in *Solar Energy Pocket Reference*, 2017.

[37] D. G. Gilmore, W. K. Stuckey, and M. Fong, “Thermal Surface Finishes,” in *Spacecraft Thermal Control Handbook*, 2002.

[38] NASA, “Cosmic Background Explorer,” Goddard Space Flight Center. Accessed: Jan. 07, 2024. [Online]. Available: https://lambda.gsfc.nasa.gov/product/cobe/

[39] Y. Lu, Q. Shao, H. Yue, and F. Yang, “A Review of the Space Environment Effects on Spacecraft in Different Orbits,” *IEEE Access*. Institute of Electrical and Electronics Engineers Inc., 2019. doi: 10.1109/ACCESS.2019.2927811.

[40] B. A. Banks, K. K. De Groh, and S. K. Miller, “Low Earth Orbital Atomic Oxygen Interactions With Spacecraft Materials,” in *2004 NASA Fall Meeting*, 2004. [Online]. Available: http://www.sti.nasa.gov

[41] M. Naumochkin, G. H. Park, K. Nielsch, and H. Reith, “Study of the Annealing Effects of Sputtered Bi2Te3 Thin Films with Full Thermoelectric Figure of Merit

Characterization," *Physica Status Solidi - Rapid Research Letters*, vol. 16, no. 4, Apr. 2022, doi: 10.1002/pssr.202100533.

[42] A. J. Paleo *et al.*, "Carbon Nanotube–Polyurethane Composite Sheets for Flexible Thermoelectric Materials," *ACS Appl Nano Mater*, Sep. 2023, doi: 10.1021/acsanm.3c03247.

[43] Almeco Group, "TiNOX energy." Accessed: Feb. 14, 2024. [Online]. Available: https://www.almecogroup.com/en/pages/479-absorbers

[44] RS PRO, "Thermocouples RS PRO Type K." Accessed: Mar. 07, 2024. [Online]. Available: https://uk.rs-online.com/

[45] Joint Committee for Guides in Metrology, "Evaluation of measurement data-Guide to the expression of uncertainty in measurement," 2008. [Online]. Available: www.bipm.org

[46] Colorado State University, "Cryogenic Safety," 2019. Accessed: Mar. 07, 2024. [Online]. Available: https://lasers.colostate.edu

[47] F. Miglietta, *Elementi di fisica tecnica*. Pitagora Editrice Bologna, 2017.

[48] P. A. Sharma, T. Ohta, M. T. Brumbach, J. D. Sugar, and J. Michael, "Ex Situ Photoelectron Emission Microscopy of Polycrystalline Bismuth and Antimony Telluride Surfaces Exposed to Ambient Oxidation," *ACS Appl Mater Interfaces*, Apr. 2021, doi: 10.1021/acsami.0c22725.

[49] D. G. Gilmore, *Spacecraft thermal control handbook*. Aerospace Press, 2002.

[50] E. T. Malroy, "Free Molecular Heat Transfer Programs for Setup and Dynamic Updating the Conductors in Thermal Desktop," 2007.

[51] Ansys Innovation Courses, "Intro to Thermal Radiation," *Ansys*. 2020. Accessed: Feb. 07, 2024. [Online]. Available: https://courses.ansys.com/wp-content/uploads/2020/05/Lesson-1-Intro-to-Thermal-Radiation.pdf

Acknowledgements

I would like to express my gratitude to Professor Lorenzini for his support throughout this project and for assisting me in establishing the connections that made my Erasmus thesis possible. I am thankful to Professor Tajmar for providing me with the opportunity to delve into this topic, and to Leo for being the best supervisor I could have hoped for.